Engineering Fracture Mechanics 216 (2019) 106370

Contents lists available at ScienceDirect

Engineering Fracture Mechanics

journal homepage: www.elsevier.com/locate/engfracmech

Accurate configuration force evaluation via hp-adaptive discontinuous Galerkin finite element analysis

Robert Bird, William M. Coombs, Stefano Giani

Department of Engineering, Durham University, Science Site, South Road, Durham DH1 3LE, UK

ARTICLE INFO

Keywords:
Configurational force
Brittle fracture
Error estimate
Discontinuous Galerkin

ABSTRACT

Engineers require accurate determination of the configurational force at the crack tip, and corresponding stress intensity factors, for fracture fatigue analysis and accurate crack propagation. However, obtaining highly accurate crack tip configuration force values is challenging with methods requiring knowledge of the stress field around the crack tip *a priori*. This paper proposes a method which aims to remove the necessity of knowing the stress field *a priori* whilst producing very accurate values of the configurational force at a static crack tip. The proposed method is demonstrated to be path independent and is combined with a robust *a posteriori* residual error estimator which is indicative of the accuracy of the configurational force calculation. This makes it possible to generate accurate values for the configurational force acting both perpendicular and parallel to the crack edges. Accuracies are achieved which are at least 10^4 times more accurate than other numerical methods which make no assumption about the local tip stress field. Therefore accurate benchmarks are determined in this paper for inclined, split and tree crack problems. In addition the new method is shown to obtain very similar values for the configurational force compared to results obtained using other methods which require knowledge of the stress field at the crack tip. The techniques presented in this paper open the door to configurational force-based methods being used for fatigue analysis.

1. Introduction

The accurate determination of configurational forces (CF) for fracture mechanics problems is essential in order to obtain realistic predictions of fatigue life, by virtue of the stress intensity factors (SIFs), as well as determining accurate propagation paths. The power released by a crack is the product of two components; the CF (or material force) and the crack tip's configurational velocity (or crack propagation rate). Maugin has made significant contributions to the theory of CF's, and the theory of CF driven brittle fracture, see the non-exhaustive list [49,55,47,48] with significant work also provided by Gurtin, [27,26]. CFs have also used to drive mesh r-adaptivity by minimisation of the internal energy of the solution with respect to a problem's nodal configuration, see for example [9,78,75]. One of the most popular ways to determine the CF, and the corresponding stress intensity factors, is through the J-integral [61] in conjunction with the interaction integral [83] which requires a known auxiliary stress field which is dependent on the material type. Alternative methods to determine the stress intensity factors include: the equivalent domain integral method [60], determining both components of the CF directly using the near tip stress solution [17,70], the virtual crack extension method [31], virtual crack closure technique [64], or by considering the nodal CF at the crack tip in the context of a finite element CF mechanics [51]. Eischen [17] presented a method to evaluate the second component of the CF by splitting the crack face integral into two separate integrals. The first integral considered the crack faces but did not include a region at the crack tip, the region at the crack tip

E-mail address: robert.e.bird@durham.ac.uk (R. Bird).

https://doi.org/10.1016/j.engfracmech.2019.02.029
Received 22 November 2018; Received in revised form 19 February 2019; Accepted 21 February 2019
Available online 16 May 2019

Nomenclature

Symbols

a, b	crack lengths
A	domain area around crack tip
$\mathscr{B}$	bounded polygonal domain
c_η, C_η, C_Σ	positive constants
$\mathcal{C}^{(\cdot)}$	continuity of a function
$\boldsymbol{D}$	material stiffness tensor
E	Young's modulus
E_m	error measure for crack face $m \in \{1, 2\}$
F	element edge
F_D	edge on Dirichlet boundary
$\mathcal{F}_B$	set of boundary edges
$\mathcal{F}_I$	set of interior edges
F_K	affine mapping
F_N	edge on Neumann boundary
F_T	edge on slip boundary
$\boldsymbol{g}_D$	applied displacement on Dirichlet BC
$\boldsymbol{g}_N$	applied traction on Neumann BC
$\boldsymbol{g}_T$	applied displacement on roller BC
$\boldsymbol{G}$	crack tip configurational force
$\boldsymbol{G}_h^{\Gamma\setminus R}$	novel CF calculation
$\boldsymbol{G}_h^D$	domain CF with no surface term
$\boldsymbol{G}_h^t$	crack tip CF
h_F	length of edge F
$\boldsymbol{h}$	divergence of displacement
$\boldsymbol{I}$	Identity matrix
K	element in $\mathcal{T}$
K_I	mode I SIF
K_{II}	mode II SIF
$\overline{K}$	reference element
L, H, W	lengths of problem domains
$\boldsymbol{m}$	normal vector to integral curve around a crack
$\boldsymbol{n}$	normal vector
n_K	node of element K
n_b	set of nodes contained within A
$\boldsymbol{n}^{\parallel}$	tangent vector
N_{n_K}	shape function for node n_K
$\mathcal{P}_{p_K}$	linearly independent set of polynomials
p_F	polynomial order of edge F
p_K	polynomial order of element K
$\underline{p}$	polynomial degree vector of mesh $\mathcal{T}$
$\mathbb{R}$	set of real numbers
R	portion of crack faces ignored in $\boldsymbol{G}_h^{\Gamma\setminus R}$
R_K	refinement level of element K
$\underline{R}$	refinement level vector of mesh $\mathcal{T}$
S	mesh refinement number
$\boldsymbol{t}(\cdot)$	traction vector
$\mathcal{T}$	mesh consisting of elements K
$\mathcal{T}^c$	subdomain of mesh at crack tip
$\mathcal{T}_H$	set of elements to refine in h
$\mathcal{T}_p$	set of elements to refine in p
$\boldsymbol{u}$	displacement vector
$\boldsymbol{V}$	configurational velocity vector
$\boldsymbol{V}_{\partial\Gamma}$	configurational velocity at the crack tip
$\boldsymbol{w}$	test function
$W_{\underline{p}}$	SIPG finite element space
$\boldsymbol{x}$	Cartesian coordinate vector
$\{\boldsymbol{g}_I\}$	nodal configurational forces
(u, v)	displacement components in x and y
(x, y)	Cartesian coordinate components
$\{\boldsymbol{V}_I\}$	vector of configurational velocity constants
$[\boldsymbol{B}_I]$	matrix of shape function derivatives
$[\boldsymbol{N}_I]$	matrix of shape functions
γ	SIPG penalty parameter
δ_1	lower bound for *hp*-adaptive marking scheme
δ_2	upper bound for *hp*-adaptive marking scheme
$\partial\mathscr{B}$	Boundary of $\mathscr{B}$
$\partial\mathscr{B}_D$	Dirichlet boundary
$\partial\mathscr{B}_N$	Neumann boundary
$\partial\mathscr{B}_{NO}$	homogeneous Neumann boundary
$\partial\mathscr{B}_T$	roller boundary
∂K	boundary of element K
$\partial\Gamma$	crack tip
$\partial\Gamma^+ \cup \partial\Gamma^-$	pair of crack faces
$\boldsymbol{\varepsilon}$	small strain tensor
η	error estimator for mesh $\mathcal{T}$
η^c	error estimator at crack tip
$\bar{\eta}^c$	set of error estimates at crack tips
$\eta_{F,K}$	external edge component of error estimator
$\eta_{J,K}$	internal edge component of error estimator
η_K	element error estimate for element K
$\eta_{\max}$	maximum error estimate for $\forall\ K \in \mathcal{T}$
$\eta_{R,K}$	area component of error estimator
θ	crack angle
λ	maximum eigenvalue of $\boldsymbol{D}$
ν	Poisson's ratio
$\boldsymbol{\sigma}$	Cauchy stress
$\boldsymbol{\sigma}_W$	Westergaard stress solution
σ_∞	far field plane stress
$\boldsymbol{\Sigma}$	Eshelby stress
$\sum$	summation operator
τ_∞	far field shear stress
$\{\boldsymbol{\Sigma}\}$	Eshelby stress vector

Acronyms

BC	boundary condition
CF	configurational force
DOF	degrees of freedom
DG	discontinuous Galerkin
LHS	left hand side
NDOF	number of degrees of freedom
RHS	right hand side
SIFs	stress intensity factors
SIPG	symmetric interior penalty discontinuous Galerkin
XBEM	extended boundary element method
XFEM	extended finite element method

Superscripts

$(\cdot)^+$	variable corresponding to K^+ on edge F
$(\cdot)^-$	variable corresponding to K^- on edge F
$\widehat{(\cdot)}$	new mesh component generated from *hp*-adaptivity

Subscripts

$(\cdot)_h$	finite element approximation of a variable

Operators

$a(\cdot,\cdot)$	LHS of SIPG bilinear form	$\lvert\cdot\rvert$	norm
$H(\cdot)$	homogeneous refinement operator	$\lVert\cdot\rVert_{0,(\cdot)}$	L2 norm
$l(\cdot)$	RHS of SIPG bilinear form	$\lvert\lvert\lvert\cdot\rvert\rvert\rvert$	SIPG norm
$[\![\cdot]\!]$	jump operator	$\{\{\cdot\}\}$	average operator
		$\nabla\cdot(\cdot)$	Cartesian differential vector

was evaluated by the second integral. Using the near tip stress solution it was shown that the value of the second integral is a function of the length of the crack face integrated over, the mode II SIF and a stress value [17], also referred to as the T-stress [62]. The second component of the CF can be determined by the method presented by [17]. Alternatively the T-stress component could be calculated using the interaction integral as shown by [72]. When the methodology to determine the T-stress provided by [17] is combined with an enrichment of the near tip stress solution, accurate results for the determination of the CF have been achieved with XBEM [71], XFEM convergence studies have also been performed by [41].

To the best of the author's knowledge, the most accurate method to determine the CF directly at the crack tip based on nodal CF values is by [14]. In that paper, CF calculations with errors in the region of 0.01% were obtained. In the case where only the CF at the crack tip node is considered, errors of $\approx$ 3% have been achieved [52,51]. For a homogeneous isotropic material with no loading on the crack faces, and no body force, both components of the CF at the crack tip can be determined from SIFs [34], the first term of which is the same as the J-integral. Accurate values for the SIFs for homogeneous isotropic materials were found using the extended boundary element method (XBEM) with the J-integral. With this method errors of $\approx 1 \times 10^{-5}$% were achieved by [3,29]. However the XBEM method is an enrichment method where the enrichment function is dependent on the material type which is not trivial to determine for general anisotropic or heterogeneous materials. Alternatively, typical errors of the SIFs produced by using the extended finite element method (XFEM), in conjunction with the interaction integral, are in the region of <0.5% [5,45], with errors of $\approx$ 0.1% achieved by [80]. If the enrichment functions are correctly determined and implemented for a crack tip problem, uniform *h*-refinement will regain polynomial convergence on the stress and displacement fields of order p and $p+1$ respectively, where p is the element basis function order. See for example the discussions of the effect of enrichment functions at crack tip singularities on convergence rates in the non-exhaustive list: [23,44,43,76]. Accurate solutions of the stress intensity factors have also been achieved by the fractural-like finite element method [79] and the Petrov-Galerkin natural element method [11]. These techniques all require some knowledge of the stress field at the crack tip *a priori*.

The stress field near a the crack tip for brittle materials is inherently singular and therefore difficult to compute accurately using finite element methods [35]. Barsoum [4] presented one of the earliest methods used to capture the stress singularity by making the Jacobian matrix, and therefore the corresponding stresses, of an element singular at the crack tip with the quarter point element. In 1999 Belytschko et al. [5] presented an enrichment method for fracture mechanics using finite elements which would later come to be known as the XFEM. Similar methods were also presented by [54,81]. The XFEM removed the necessity for the element geometry to conform to the crack edges by including jumps in displacements and stresses within elements. XFEM also improved the representation of the stress field at the crack tip by including singular terms derived from the near tip displacement field [35] to determine stress intensity values. The approach has also been applied directly to determine the CF by Fagerström et al. [40,22]. A discontinuous Galerkin XFEM method capable of achieving optimal convergent results has also been produced by Shen *el al.* [68].

The stress solution, and therefore the evaluation of the J-integral and stress intensity factors, of a problem modelled using finite elements can be improved by using a *h*-adaptive, *p*-adaptive or *hp*-adaptive methods. *A posterori* error estimates can be used in conjunction with adaptivity techniques to estimate the global errors, or errors of specific features, of a problem. Within the context of fracture mechanics one of the earliest works of using *h*-adaptivity is presented by [53], here only the global error was improved, the error associated with the J-integral integral at the crack tip was not quantified. More recently, Stein et al. [65,66] made a significant contribution to error driven fracture analysis through the use of a goal-orientated error estimator to provide an estimation of the J-integral accuracy and to flag elements for *h*-refinement. The adaptivity approach of the analysis was further improved upon by [30]. Using error analysis for fracture problems has also been extended to XFEM by using a global recovery method [8,15], which quantifies the error between the enriched and non-enriched solution to estimate the error in stress solution about the crack tip. In a similar fashion the Zienkiewicz and Zhu *a posteriori* error estimator [84] has been used to drive *h*-refinement in fracture problems modelled using the continuous Galerkin finite element method [56,38]. The most popular technique to improve the accuracy of the stress around the crack for finite elements is to use a goal orientated *a posteriori* error, such as in [67,39,74,57,24] amongst others. A numerical example of using residual based *a posteriori* error estimates to drive *h*-adaptive algorithms for problems containing cracks was shown by Cirack et al. [13]. However, there were a number of limitations in the analysis: (i) there was no investigation into how the CF improved, (ii) only the first component of the CF was considered, (iii) there was no comparison to an analytical solution, and (iv) only polynomial convergence was achieved. Last, direct evaluation of nodal CF values has also been used to improve the stress solution of crack problems, in *hr*- and *r*-adaptive methods [59,78].

Many of the papers cited in this introduction improve the stress solution effectively at the crack tip. However in computing the CF, J-integral or SIFs, assumptions, which are valid, are made about the stress field near the crack tip. This paper has three key contributions:

- Firstly a rigorous *hp a posteriori* error estimator [7] is combined with a *hp*-adaptive scheme, [16], to achieve very accurate values for both components of the CF for linear elastic homogeneous isotropic problems. The error estimate is shown to bound the error

in the CF component acting parallel to the crack edges and is shown numerically to converge at a similar rate to the CF component acting perpendicular to the crack edges. The error estimate also dictates which elements should be marked for *h*- and *p*-refinement.

- Secondly the difficulty in modelling stress singularities on the boundaries is discussed. A simple and effective novel method is proposed to evaluate the CF directly on the boundary is developed, where no *a priori* knowledge of the stress tip singularity is required. This provides potential for the proposed method to act as a black box with the capability to be applied to a range of materials.
- Thirdly since the error estimate is an *a posteriori* residual based error estimator, and is shown to bound the error in the CF there is no need to solve an adjoint problem for each refinement step, which is the case for goal-orientated error estimates.

The fracture problems are cast within a discontinuous Galerkin (DG) finite element scheme as DG schemes are highly suited to *hp*-adaptivity due to the simple communication at element interfaces. The *hp*-adaptive method achieves exponential convergence of the both the error estimate and the error in both components of the CF. The proposed method is shown to be domain independent and the relationship between the convergence of the error in the CF and the error estimate value is demonstrated.

The paper is split into 5 further sections. Section 2 presents the symmetric internal penalty discontinuous Galerkin (SIPG) method, its corresponding *a posteriori* error estimate and the error driven *hp*-adaptive scheme. Section 3 demonstrates that it is possible to bound the error in the area integral component of the CF calculation by the error estimator. The section then proceeds to show, and discuss why, the CF calculation is domain dependent if the line integral along the crack edges of the CF calculation is excluded and why these crack edge terms are difficult to evaluate. This information is used in Section 4 to propose a new method to determine the CF at the crack tip followed by Section 5 which provides examples of the accuracy obtainable and the domain independence of the method. Finally, conclusions are drawn in Section 6.

2. Linear elastic formulation

This section begins by presenting the strong form statement of equilibrium for linear elasticity with corresponding boundary conditions. The problem domain is then subdivided into elements to form a mesh in which the SIPG formulation is cast. An *a posteriori* error estimate is then presented for the SIPG method.

2.1. Symmetric interior penalty method

The problem modelled in this paper is small strain linear elasticity. Let $\mathscr{B}_\Gamma$ be a bounded polygonal domain in $\mathbb{R}^2$ with the boundary $\partial\mathscr{B}_\Gamma = \partial\mathscr{B}_D \cup \partial\mathscr{B}_N \cup \partial\mathscr{B}_T$, where $\partial\mathscr{B}_D \cap \partial\mathscr{B}_N \cap \partial\mathscr{B}_T = \varnothing$. The strong form statement of equilibrium and the boundary conditions are defined as

$$\begin{aligned}
&\nabla\cdot\boldsymbol{\sigma}(\boldsymbol{u}) = \boldsymbol{0} \quad \text{in} \quad \mathscr{B}_\Gamma,\\
&\boldsymbol{u} = \boldsymbol{g}_D \quad \text{on} \quad \partial\mathscr{B}_D,\\
&\boldsymbol{\sigma}(\boldsymbol{u})\cdot\boldsymbol{n} = \boldsymbol{g}_N \quad \text{on} \quad \partial\mathscr{B}_N,\\
&(\boldsymbol{\sigma}(\boldsymbol{u})\boldsymbol{n})\cdot\boldsymbol{n}^{\parallel} = \boldsymbol{0} \quad \text{on} \quad \partial\mathscr{B}_T,\\
&\boldsymbol{u}\cdot\boldsymbol{n} = \boldsymbol{g}_T\cdot\boldsymbol{n} \quad \text{on} \quad \partial\mathscr{B}_T,
\end{aligned} \tag{1}$$

where the Dirichlet boundary condition is applied on $\partial\mathscr{B}_D$, the Neumann boundary condition is applied on $\partial\mathscr{B}_N$ and the mixed Neumann/Dirichlet boundary condition is applied on $\partial\mathscr{B}_T$ (more commonly referred to as a roller boundary condition). $\boldsymbol{u} = (u, v) \in \mathbb{R}^{2\times1}$ is displacement and $\boldsymbol{\sigma}(\boldsymbol{u}) \in \mathbb{R}^{2\times2}$ is the Cauchy stress matrix. $\boldsymbol{\sigma}(\boldsymbol{u}) = \boldsymbol{D}$: $\boldsymbol{\varepsilon}(\boldsymbol{u})$, where $\boldsymbol{D} \in R^{2\times2\times2\times2}$ is the material stiffness tensor and the small strain matrix $\boldsymbol{\varepsilon} \in \mathbb{R}^{2\times2}$ is

$$\boldsymbol{\varepsilon}(\boldsymbol{u}) = \begin{bmatrix} \frac{\partial u}{\partial x} & \frac{1}{2}\left(\frac{\partial v}{\partial x} + \frac{\partial u}{\partial y}\right) \\ \frac{1}{2}\left(\frac{\partial v}{\partial x} + \frac{\partial u}{\partial y}\right) & \frac{\partial v}{\partial y} \end{bmatrix}, \tag{2}$$

where (x, y) is the Cartesian coordinate system describing $\mathscr{B}_\Gamma$. On the set of all boundaries $\partial\mathscr{B}_\Gamma$ there exists the outward normal $\mathbf{n}$ and corresponding tangent $\mathbf{n}^{\parallel}$. $\boldsymbol{g}_D$ and $\boldsymbol{g}_T$ are the applied displacements on $\partial\mathscr{B}_D$ and $\partial\mathscr{B}_T$ respectively; $\boldsymbol{g}_N$ is the applied traction on $\partial\mathscr{B}_N$

The domain $\mathscr{B}_\Gamma$ is subdivided by the mesh $\mathcal{T}$ consisting of elements K; $\mathcal{T}$ is in general irregular. $K \in \mathcal{T}$ is the image of the reference triangle $\overline{K}$ under an affine elemental mapping F_K: $\overline{K} \to K$. $\mathcal{F}(K)$ is the set of the elemental edges of an element K. If the intersection $F = \partial K \cap \partial K'$ exists then F is an interior edge of $\mathcal{T}$ with the set of all interior edges denoted by $\mathcal{F}_I(\mathcal{T})$. Analogously, if the intersection $F = \partial K \cap \partial\mathscr{B}_\Gamma$ of an element $K \in \mathcal{T}$ and $\partial\mathscr{B}_\Gamma$ is a segment, we call F a boundary edge of $\mathcal{T}$. The set of all boundary edges of $\mathcal{T}$ is denoted by $\mathcal{F}_B(\mathcal{T})$ and it is the union of the three sets $\mathcal{F}_N(\mathcal{T})$, $\mathcal{F}_D(\mathcal{T})$ and $\mathcal{F}_T(\mathcal{T})$ of edges on the three boundaries $\partial\mathscr{B}_N$, $\partial\mathscr{B}_D$ and $\partial\mathscr{B}_T$ respectively. The two elements sharing an interior edge F are denoted arbitrarily K^+ and K^- with their corresponding variables given the same + or − superscript. Given this notation, jumps across element boundaries are defined as

$$[\![\boldsymbol{w}]\!] = \boldsymbol{w}^+\mathbf{n}^+ - \boldsymbol{w}^-\mathbf{n}^+, \tag{3}$$

which when expanded becomes

$$\left[\!\left[\boldsymbol{w}\right]\!\right] = \begin{Bmatrix} w^+(1) \\ w^+(2) \end{Bmatrix} \begin{bmatrix} n^+(1) n^+(2) \end{bmatrix} - \begin{Bmatrix} w^-(1) \\ w^-(2) \end{Bmatrix} \begin{bmatrix} n^+(1) n^+(2) \end{bmatrix},$$

and averages across element edges are

$$\left\{\boldsymbol{\sigma}(\boldsymbol{w})\right\} = \frac{1}{2}(\boldsymbol{\sigma}(\boldsymbol{w})^+ + \boldsymbol{\sigma}(\boldsymbol{w})^-). \tag{4}$$

For each element $K \in \mathcal{T}$, we define p_K as the polynomial order. We also define the vector function $\underline{p} = \{ p_K \,:\, K \in \mathcal{T} \}$. For any mesh $\mathcal{T}$ of $\mathscr{B}_\Gamma$ with the degree vector $\underline{p}$, we then define the *hp*-version discontinuous Galerkin finite element space by,

$$W_{\underline{p}}(\mathcal{T}) = \{ \boldsymbol{w} \in [L^2(\mathscr{B}_\Gamma)]^2 \,:\, \boldsymbol{w}|_K \in [\mathcal{P}_{p_K}(K)]^2,\ K \in \mathcal{T} \}$$

where $[\mathcal{P}_{p_K}(K)]^2 \in \mathbb{R}^2$ is a linearly independent set of polynomials which form a polynomial basis, of order p_K, on the reference triangle $\overline{K}$, provided by Solin [73].

The SIPG method in the bilinear form is introduced for the approximation of the model problem (1). Find $\boldsymbol{u}_h \in W_{\underline{p}}(\mathcal{T})$, such that,

$$a(\boldsymbol{u}_h, \boldsymbol{w}) = l(\boldsymbol{w}), \quad \forall \boldsymbol{w} \in W_{\underline{p}}(\mathcal{T}) \tag{5}$$

where the bilinear forms are,

$$\begin{aligned} a(\boldsymbol{u}, \boldsymbol{w}) := & \sum_{K \in \mathcal{T}} \int_K \boldsymbol{\sigma}(\boldsymbol{u}) : \boldsymbol{\varepsilon}(\boldsymbol{w})\, d\mathbf{x} \\ & - \sum_{F \in \mathcal{F}_I(\mathcal{T}) \cup \mathcal{F}_D(\mathcal{T})} \int_F \{\boldsymbol{\sigma}(\boldsymbol{u})\} \cdot [\![\boldsymbol{w}]\!] + \{\boldsymbol{\sigma}(\boldsymbol{w})\} \cdot [\![\boldsymbol{u}]\!]\, ds \\ & + \sum_{F \in \mathcal{F}_I(\mathcal{T}) \cup \mathcal{F}_D(\mathcal{T})} \frac{\gamma p_F^2}{h_F} \int_F [\![\boldsymbol{u}]\!] \cdot [\![\boldsymbol{w}]\!]\, ds \\ & - \sum_{F \in \mathcal{F}_T(\mathcal{T})} \int_F (\mathbf{t}(\boldsymbol{u}) \cdot \mathbf{n})(\boldsymbol{w} \cdot \mathbf{n}) + (\mathbf{t}(\boldsymbol{w}) \cdot \mathbf{n})(\boldsymbol{u} \cdot \mathbf{n})\, ds \\ & + \sum_{F \in \mathcal{F}_T(\mathcal{T})} \frac{\gamma p_F^2}{h_F} \int_F (\boldsymbol{u} \cdot \mathbf{n})(\boldsymbol{w} \cdot \mathbf{n})\, ds\ , \end{aligned} \tag{6}$$

$$\begin{aligned} l(\boldsymbol{w}) := & - \sum_{F \in \mathcal{F}_D(\mathcal{T})} \int_F \mathbf{g}_D \cdot \mathbf{t}(\boldsymbol{w})\, ds + \sum_{F \in \mathcal{F}_D(\mathcal{T})} \frac{\gamma p_F^2}{h_F} \int_F \mathbf{g}_D \cdot \boldsymbol{w}\, ds \\ & - \sum_{F \in \mathcal{F}_N(\mathcal{T})} \int_F \mathbf{g}_N \cdot \boldsymbol{w}\, ds \\ & - \sum_{F \in \mathcal{F}_T(\mathcal{T})} \int_F (\mathbf{g}_T \cdot \mathbf{n})(\mathbf{t}(\boldsymbol{w}) \cdot \mathbf{n})\, ds + \sum_{F \in \mathcal{F}_T(\mathcal{T})} \frac{\gamma p_F^2}{h_F} \int_F (\mathbf{g}_T \cdot \mathbf{n})(\boldsymbol{w} \cdot \mathbf{n}) ds. \end{aligned} \tag{7}$$

where γ is the SIPG constant and is chosen here to have a value of $10 \times \lambda$, where λ is the maximum eigenvalue of the material matrix $\boldsymbol{D}$, [28,18,19]. The displacement and stress field solutions, obtained using SIPG, converge optimally if γ is sufficiently high enough; see the *a priori* error estimate derivation for elliptic problems in [58]. The choice of 10 is to ensure that γ is always high enough, and therefore that optimal convergence is achieved, [33]. The value 10 is not unique to linear elastic problems, rather for elliptic problems modelled using SIPG, for example see [1]. For linear elasticity wide ranging values in the stiffness tensor $\boldsymbol{D}$ are possible, γ therefore includes values of $\boldsymbol{D}$ in its definition such that its value changes accordingly to ensure optimal convergence [28]. $\mathbf{t}(\cdot) = \boldsymbol{\sigma}(\cdot) \cdot \mathbf{n}$ is a general description of a traction that is not the on boundary $\partial\mathscr{B}_N$, the edge polynomial, p_F, is described as,

$$p_F = \begin{cases} \max\left(p_K^+, p_K^-\right), & \text{if on the internal edges,} \quad F = \partial K^+ \cap \partial K^- \in \mathcal{F}_I(\mathcal{T}), \\ p_K, & \text{if on the external edges,} \quad F = \partial K \cap \partial\mathscr{B}_\Gamma \in \mathcal{F}(\mathcal{T}) \setminus \mathcal{F}_I(\mathcal{T}), \end{cases} \tag{8}$$

and h_F is the length of the segment F. In SIPG the degrees of freedom are element specific. Instead of sharing degrees of freedom, as in continuous Galerkin methods, the elements interact through two edge integral terms (6) performed on the interior edges $\mathcal{F}_I$. The first edge term, appearing as the second integral in (6), averages the tractions acting between elements so the same traction acts on the elements sharing an interface, it also contains a symmetrising term which ensures optimal convergence for the given polynomial order of the elements in the mesh. The second edge term, appearing as the third integral in (6), penalises displacements between elements to stabilise the method. Since elements interact through edge integrals, implementing adjacent elements with relative differences in polynomial order and edge length, such that the mesh is non-conforming, is straightforward. This feature of discontinuous Galerkin (DG) methods is useful for *hp*-adaptive methods where element size and polynomial order can vary significantly within a mesh.

2.2. Error estimate

The derivation of a *hp a posteriori* residual based error estimate for SIPG is complex and is not the main focus of the paper. The derivation is therefore not included in this paper and only a description of the role of each term is provided here. However, a complete derivation can be found in [7]. The error estimate η is both reliable and efficient for the error in the DG energy norm, that is

$$c_\eta \eta \leq |||\boldsymbol{u} - \boldsymbol{u}_h|||_{\mathcal{T}} \leq C_\eta \eta \tag{9}$$

where C_η and c_η are two positive constants independent of the element size, element polynomial order, and magnitude of the loading applied on the boundary [7]. $\boldsymbol{u}$ is the true displacement solution, and the DG norm is

$$|||\boldsymbol{u}|||_{\mathcal{T}} := \left(\sum_{K\in\mathcal{T}} \|\nabla \boldsymbol{u}\|^2_{0,K} + \sum_{F\in\mathcal{F}_{\mathrm{I}}(\mathcal{T})} \frac{\gamma p_F^2}{h_F} \left\| [\![\boldsymbol{u}]\!] \right\|^2_{0,F} + \sum_{F\in\mathcal{F}_{\mathrm{D}}(\mathcal{T})} \frac{\gamma p_F^2}{h_F} \left\| \boldsymbol{u} \right\|^2_{0,F} + \sum_{F\in\mathcal{F}_{\mathrm{T}}(\mathcal{T})} \frac{\gamma p_F^2}{h_F} \left\| \boldsymbol{u}\cdot\mathbf{n} \right\|^2_{0,F} \right)^{1/2}, \tag{10}$$

When η is combined with a suitable *hp*-adaptive scheme, exponential convergence of the error estimate is achieved with the number of degrees of freedom in the system. Since η is both reliable and efficient for the error in the DG norm (9), the error in the DG norm also convergences exponentially. The global error estimate η is defined as,

$$\eta = \sqrt{\sum_{K\in\mathcal{T}} \left(\eta^2_{R,K} + \eta^2_{J,K} + \eta^2_{F,K} \right)} \tag{11}$$

where a single element error estimate is $\eta^2_K = \eta^2_{R,K} + \eta^2_{J,K} + \eta^2_{F,K}$. The first component of η^2_K is an area integral, defined as

$$\eta^2_{R,K} = \frac{h_K^2}{p_K^2} \|\nabla\cdot\boldsymbol{\sigma}(\boldsymbol{u}_h)\|^2_{0,K}, \tag{12}$$

where h_K is the diameter of element K. $\eta^2_{R,K}$ measures how well the strong form statement of equilibrium $\nabla\cdot\boldsymbol{\sigma}(\boldsymbol{u}_h) = \boldsymbol{0}$ applied specifically here to a linear elastic problem has been satisfied by the finite element approximation of the weak formulation (1).

The solution to the DG method does not necessarily satisfy $\mathcal{C}^0$ across element edges, therefore jumps in displacement can exist between elements on the segment $F \in \mathcal{F}_I(\mathcal{T})$. Both mixed and pure Dirichlet boundary conditions are imposed weakly, so jumps in displacement also exist between the displacement solution on the element boundary and the boundary condition imposed on them. Since the true solution for displacement is continuous along these boundaries, the error in the jump in displacement on the segment $F \in \mathcal{F}_I(\mathcal{T})$, the pure Dirichlet boundary $F \in \mathcal{F}_D(\mathcal{T})$ and the mixed Neumann/Dirichlet boundary $F \in \mathcal{F}_I(\mathcal{T})$ are measured as

$$\eta^2_{J,K} = \frac{1}{2} \sum_{F\in\mathcal{F}_I} \frac{\gamma^2 p_F^3}{h_F} \left\| [\![\boldsymbol{u}_h]\!] \right\|^2_{0,F} + \sum_{F\in\mathcal{F}_D} \frac{\gamma^2 p_F^3}{h_F} \left\| \boldsymbol{u}_h - \mathbf{g}_D \right\|^2_{0,F} + \sum_{F\in\mathcal{F}_{\mathrm{T}}} \frac{\gamma^2 p_F^3}{h_F} \left\| \boldsymbol{u}_h\cdot\mathbf{n} - \mathbf{g}_T\cdot\mathbf{n} \right\|^2_{0,F} \tag{13}$$

Like most finite element methods, SIPG does not satisfy $\mathcal{C}^1$ across edges of adjacent elements $F \in \mathcal{F}_I(\mathcal{T})$. For element edges on the pure Neumann boundary $F \in \mathcal{F}_N(\mathcal{T})$, and for element edges on the mixed Neumann boundary, $F \in \mathcal{F}_I(\mathcal{T})$, these errors are measured through

$$\eta^2_{F,K} = \frac{1}{2} \sum_{F\in\mathcal{F}_I} \frac{h_F}{p_F} \left\| [\![\boldsymbol{\sigma}(\boldsymbol{u}_h)]\!] \right\|^2_{0,F} + \sum_{F\in\mathcal{F}_N} \frac{h_F}{p_F} \left\| \boldsymbol{\sigma}(\boldsymbol{u}_h)\cdot\mathbf{n} - \mathbf{g}_N \right\|^2_{0,F} + \sum_{F\in\mathcal{F}_T(K)} \frac{h_F}{p_F} \left\| \mathbf{t}(\boldsymbol{u}_h)\cdot\mathbf{n}^{\parallel} \right\|^2_{0,F} \tag{14}$$

Last, one of the conditions for the *a posteriori* error estimate to be reliable and efficient for the error in the DG norm is the jump in polynomial order between a neighbouring pair of elements p_K^- and p_K^+ must be bound by arbitrary constant, we choose $|p_K^+ - p_K^-| \leqslant 1$. The other condition is the number of hanging nodes per element edge has to be bound, in this implementation we only allow one hanging node per element edge.

2.3. hp-Adaptivity

The *hp*-adaptive method is driven by the element estimate η^2_K calculated for all $K \in \mathcal{T}$. The *hp*-adaptive strategy was originally proposed by [32] for the boundary element method but was shown to be proficient for the FEM when the solution contains singularities [16].

The *hp*-adaptive method adapts the mesh to reduce η with the greatest efficiency with respect to the number of degrees of freedom added. The algorithm for the adaptivity method is given by Algorithm 1. The method starts with finding the element with the largest error, $\eta^2_{\max} = \max_{K\in\mathcal{T}}(\eta^2_K)$, and defining two parameters δ_2 and δ_1, where $1 \geqslant \delta_2 \geqslant \delta_1 \geqslant 0$. Elements with the larger errors in the mesh, $\eta^2_K > \delta_2\eta^2_{\max}$, are assumed to be associated with a non-regular part of the solution. Since an arbitrarily high polynomial function will always have some error associated with modelling a non-regular function, these elements are refined in *h*. Elements with errors in the band, $\delta_2\eta^2_{\max} \geqslant \eta^2_K > \delta_1\eta^2_{\max}$, are considered to be modelling a regular part of the solution, but p_K is not high enough to obtain a good solution and so a relatively large value of η^2_K still exists. Since the solution is assumed to be regular it is more efficient here to refine in polynomial order than in *h*. Although refining in *h* will achieve convergence, it will be slower with respect to the number of degrees of freedom added.

Algorithm 1. *hp*-adaptive algorithm.

This algorithm describes the error driven hp-adaptive method. It is explained in conjunction with an example consisting of 6 elements, shown below. Each element has a polynomial order and refinement level, p_K and R_K respectively; these are expressed as a row vector $[p_K, R_K]$ in each element contained in the Algorithm.

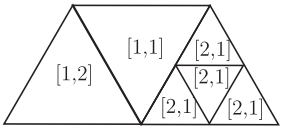

Step 1 Compute the estimated error η_K and determine the maximum element error, $\eta^2_{\max} = \max_{K\in\mathcal{T}}(\eta^2_K)$.

Step 2 Determine the set of elements to refine in p and create $\mathcal{T}_P = \{K \in \mathcal{T} | \delta_2\eta^2_{\max} \geq \eta^2_K > \delta_1\eta^2_{\max}\}$.

Step 3 Identify the set of elements to refine in h and create $\mathcal{T}_H$ of $\mathcal{T}$ such that $\mathcal{T}_H = \{K \in \mathcal{T} | \eta^2_K > \delta_2\eta^2_{\max}\}$.

Step 4 Elements are p-refined by adding 1 to p_K if $K \in \mathcal{T}_P$, and elements are marked for h-refinement by adding 1 to R_K if $K \in \mathcal{T}_H$. This is indicated in the diagram below, the elements marked for p and h refinement are marked with light and dark grey shading respectively.

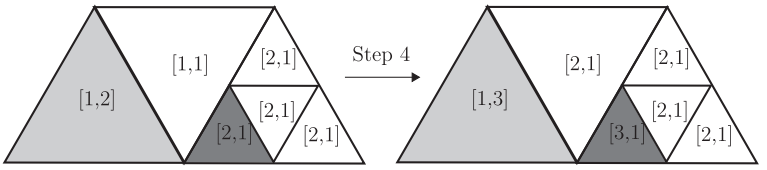

It is important to reiterate here that $K \in \mathcal{T}$ only refers to the geometry of an element, each element has an associated polynomial order p_K. A second variable for K is also defined as R_K, with the vector function $\underline{R} = \{R_K : K \in \mathcal{T}\}$. R_K is a refinement flag used to ensure that only one hanging node exists per element edge, this is necessary for (9) to hold [7]. The variable S is also introduced, it is the number of *hp*-refinement steps that have occurred. At $S = 0$ no refinement steps have occurred and the mesh is conforming such that $R_K = 0 \ \forall \ K \in \mathcal{T}$.

Step 5 To ensure that only one hanging node exists on an element edge, the absolute difference in R_K for two adjacent elements, K^+ and K^-, must be less than or equal to 1, $|R^+_K - R^-_K| \leq 1$. To facilitate this, all edges in the mesh are looped through. If $|R^+_K - R^-_K| \leq 1$ is not true for an edge the element with the smaller R_K value is: identified, its value increased by 1 and K is added to the set $\mathcal{T}_H$. The loop is only exited when a complete run through of all edges in within the mesh is completed with no changes to $R_K \in \underline{R}$. In this example only one new element is identified for h-refinement, indicated by the dark grey shaded element below.

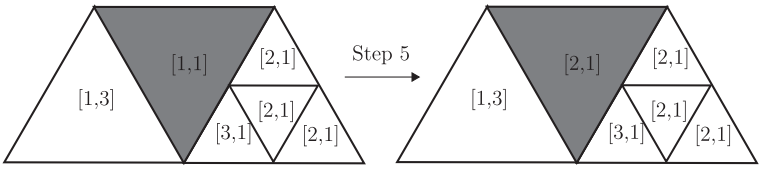

Step 6 h-refine all elements $K \in \mathcal{T}_H$ to create the new mesh $\widehat{\mathcal{T}}$.

Step 7 Another criteria of to ensure the error estimate is reliable and efficient for the true error is that the difference in polynomial order between two adjacent elements in a mesh must be less than or equal to one. To ensure this is true, all edges in the mesh are looped through. If $\left|p^+_{\widehat{K}} - p^-_{\widehat{K}}\right| \leqslant 1$ is not true for an edge the element with the smaller $p_{\widehat{K}}$ value is: identified, its value increased by 1 and $\widehat{K}$ is added to the set $\widehat{\mathcal{T}}_P$. The loop is only exited when a complete run through of all edges within the new mesh is completed with no changes to $p_{\widehat{K}} \in \underline{\widehat{p}}$. In this example two new elements are identified for p-refinement, indicated by the light grey shaded elements below.

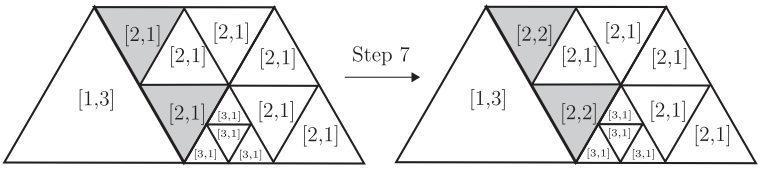

Step 8 Last, as the *hp*-adaptive algorithm is complete, the mesh number is increased by 1: $S = S + 1$.

During the *hp*-adaptive algorithm only two meshes are considered at a time, the current mesh $\mathcal{T}$ and the adapted mesh $\widehat{\mathcal{T}}$. We denote the set of elements for h-refinement as $\mathcal{T}_H \subset \mathcal{T}$ and the set of element for p-refinement as $\mathcal{T}_P \subset \mathcal{T}$. If an element is not flagged for h-refinement, $K \notin \mathcal{T}_H$, its geometry remains unchanged during h-refinement. The element therefore exists in the old and updated mesh such that $\exists \widehat{K} \in \widehat{\mathcal{T}}$, where $\widehat{K} = K$, $p_{\widehat{K}} = p_K$ and $R_{\widehat{K}} = R_K$. Otherwise if the element is flagged for refinement, $K \in \mathcal{T}_H$, the element K is subdivided into 4 new elements such that $\widehat{K} \in H(K)$, where H is denoted the set of all new elements created by the homogeneous h-refinement of K, with $p_{\widehat{K}\in H(K)} = p_K$ and $R_{\widehat{K}\in H(K)} = R_K$. The *hp*-refinement strategy, in conjunction with an example, is explained in Algorithm 1.

For problems containing a singularity it was shown choosing δ_1 and δ_2 as 0.7 and 0.07 respectively was suitable to obtain

exponential convergence of the error estimate [16]. In this paper for the crack tip singularity δ_1 and δ_2 were chosen as 0.3 and 0.07 respectively as a slightly faster exponential convergence was obtained. This routine is relatively simple to implement and is applicable directly to all types of basis functions. However, more sophisticated, but more complex, methods are available, see [16] and the references within for further details.

3. Configurational Force post processing formulation

When a crack propagates, material is split apart dissipating energy [25]. In a dynamic setting the power released by a crack tip moving through a material has an associated configurational velocity and force, often referred to as the CF or material force. The CF can be derived by considering a global formulation of the dissipation of power of a solid [51]. The derivation of the CF at the crack tip naturally produces a path integral around the crack tip where the path integral size is taken to the limit of 0. Within a numerical setting this integral cannot be evaluated, therefore an equivalent integral on a path, or domain, of finite size is required.

In two dimensions the CF at a crack tip can be evaluated by considering a finite line integral around the crack which includes integrating along the crack edges [61,17], or a line integral along the crack edges with an area integral around the crack tip [30]. Alternatively, in the context of configurational force mechanics, it was shown by [51] that the crack tip CF could be evaluated by considering the finite element CF value of the crack tip node. In this section a proof showing that the square of the error estimate is a reliable indicator for the error in the area integral contribution to the crack CF is given. As the CF convergences exponentially with error driven *hp*-adaptivity, accuracies currently unobtainable in literature for the mixed mode Westergaard problem [82] are achieved here.

Eischen [17] showed that both components of $\boldsymbol{G}$ could be made path independent if a line integral along the crack faces is included. This path integral form was recast as a domain integral form by using the divergence theorem by Raju et al. [60]. Using a similar technique to the derivation the domain variation of the J-integral achieved by Shih et al. [69]. However, as mentioned by [60,17,50,77,83] amongst others, the line integral along the crack edges is difficult to compute and results in a poor representation of the CF at the crack tip. This has lead to a number of techniques, as discussed in the Introduction, which try and avoid computing this line integral. To further understanding as to why this integral is difficult to compute a discussion on the influence of an integral on the boundary of the domain that includes a singularity is presented. These results are then used in Section 4 to develop a new technique which evaluates the crack edge terms directly as part of the CF calculation. An alternative formulation in which the crack edge integral is ignored is presented by Denzer et al. [14], however this, in general, is domain dependent.

3.1. Configurational force

The work of Eshelby [20,21], Rice [61] and Irwin [35,34], are fundamental to the original derivation the CF at the crack tip. More recently, an alternative derivation to determine the energy released by a crack propagating has been presented by Miehe et al. [51].

Following [51] the power released by a propagating crack is given by

$$\mathscr{D} = \boldsymbol{V}_{\partial\Gamma} \cdot \boldsymbol{G}, \tag{15}$$

where $\boldsymbol{V}_{\partial\Gamma}$ and $\boldsymbol{G}$ are the configurational velocity and CF at the crack tip, respectively. To maximise (15) for a propagating crack, that is not branching and is propagating as a $\mathcal{C}^1$ continuous path, the configurational velocity at the crack tip, otherwise known as the crack propagation velocity, should be co-linear to $\boldsymbol{G}$, [51]. For the numerical experiments presented here $G(1)$ refers to component of $\boldsymbol{G}$ that acts parallel to the crack lips and $G(2)$ is the perpendicular component which exists 90° anticlockwise to $G(1)$. However depending on the orientation taken as perpendicular, $G(2)$ may be negative. The definition of the CF in the continuous domain, $\boldsymbol{G}$, is valid for all problems and is defined as

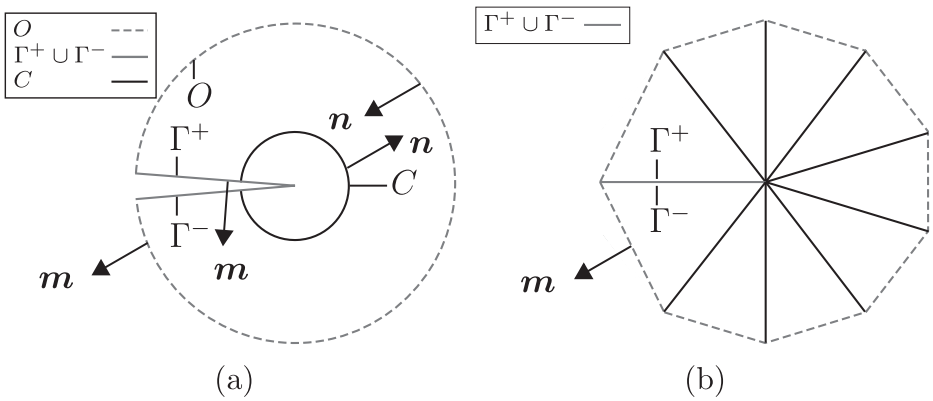

Fig. 1. Domain integration definitions: (a) continuous representation of the paths for the line integral (16) and (b) a finite element representation of the paths in a finite element discretisation of the crack tip.

$$\boldsymbol{G} = \lim_{|C|\to 0} \int_C \boldsymbol{\Sigma}\cdot\boldsymbol{n}, \tag{16}$$

where C is an integral path around the crack tip, $\partial\Gamma$, and $\boldsymbol{n}$ is the normal on the curve C, shown in Fig. 1(a). $\boldsymbol{\Sigma} = \psi(\boldsymbol{\varepsilon})\boldsymbol{I} - (\partial\boldsymbol{u}/\partial\boldsymbol{x})^{\top}\boldsymbol{\sigma}$ is the non-symmetric Eshelby stress, $\boldsymbol{I} \in \mathbb{R}^{2\times 2}$ is the identity matrix, ψ is the free energy function for linear elasticity and $\boldsymbol{x} = (x, y)$ is the Cartesian coordinate system of the undeformed material state. $\boldsymbol{G}$ is the CF at the crack tip, the first term of which is the same as the J-integral introduced by Rice [61] for straight cracks.

Within the framework of configurational mechanics and finite elements it was proposed by [51] that $\boldsymbol{G}$ can be determined by considering the nodal element CF value at the crack tip (see Fig. 1(b)) using

$$\begin{aligned}\boldsymbol{G}_h &= -\sum_{K\in A}\sum_{n_K\in n_b}\int_K [\boldsymbol{B_I}]^{\top}\{\boldsymbol{\Sigma}\}d\mathbf{x},\\ &= -\sum_{K\in A}\sum_{n_K\in n_b}\int_K \begin{bmatrix} \frac{\partial N_{n_K}}{\partial x} & 0\\ 0 & \frac{\partial N_{n_K}}{\partial y}\\ \frac{\partial N_{n_K}}{\partial y} & 0\\ 0 & \frac{\partial N_{n_K}}{\partial x}\end{bmatrix}^{\top}\begin{Bmatrix}\Sigma_{xx}\\ \Sigma_{yy}\\ \Sigma_{xy}\\ \Sigma_{yx}\end{Bmatrix}d\mathbf{x},\end{aligned} \tag{17}$$

where n_b is the crack tip node, N_{n_K} is the shape function for node n_K of the element K, A is the set of elements K which share a node with the crack tip and $\boldsymbol{B_I}$ is a matrix of shape function derivatives with respect to the undeformed material state $\mathscr{B}_{\Gamma}$. When only considering the nodal CF value at the crack tip, the calculation of $\boldsymbol{G}_h$ (17) is referred to as $\boldsymbol{G}_h^t$. A slight variation of (17) is the domain approach, discussed by [14]. It is obtained by redefining A as a set of elements which have a node within a radial distance R away from the crack tip, and n_b as the set of nodes within R. When considering the domain variation of (17), $\boldsymbol{G}_h$ (17) is referred to as $\boldsymbol{G}_h^D$. The domain size chosen to calculate $\boldsymbol{G}$ is topological. For $\boldsymbol{G}_h^t$ it is the set of elements that share a node with the crack tip, whereas for the domain size of $\boldsymbol{G}_h^D$, and for all further domain formulations, it is the area covered by the initial elements that share a node with the crack tip for the most coarse mesh in a series of mesh refinements.

Alternative domain formulations to calculate the crack CF value have been presented by [42,60,30] which use the area integral in (17) and include a line integral along the crack edges within the domain such that

$$\begin{aligned}\boldsymbol{G}_h^{\Gamma} &= -\sum_{K\in A}\sum_{n_K\in n_b}\int_K [\boldsymbol{B_I}]^{\top}\{\boldsymbol{\Sigma}\}d\mathbf{x} + \sum_{\partial K\in(\Gamma^{+}\cup\Gamma^{-})}\sum_{n_K\in n_b}\int_{\partial K}[\boldsymbol{N_I}]\left\{\psi(\boldsymbol{\varepsilon})\cdot\boldsymbol{m}\right\}ds,\\ &= -\sum_{K\in A}\sum_{n_K\in n_b}\int_K [\boldsymbol{B_I}]^{\top}\{\boldsymbol{\Sigma}\}d\mathbf{x} + \sum_{\partial K\in(\Gamma^{+}\cup\Gamma^{-})}\sum_{n_K\in n_b}\int_{\partial K}\begin{bmatrix}N_{n_K} & 0\\ 0 & N_{n_K}\end{bmatrix}\begin{Bmatrix}m(1)\psi(\boldsymbol{\varepsilon})\\ m(2)\psi(\boldsymbol{\varepsilon})\end{Bmatrix}ds,\end{aligned} \tag{18}$$

where $\boldsymbol{N_I}^{\top}$ is the matrix of the basis functions for the element K and, $m(1)$ and $m(2)$ are the Cartesian components of normal vector $\boldsymbol{m}$ in x and y, see Fig. 1(a). The line integral along the crack edges considers $\psi(\boldsymbol{\varepsilon})\cdot\boldsymbol{m}$, rather than $\boldsymbol{\Sigma}\cdot\boldsymbol{m}$. This is because the crack edges are traction free and as such

$$\boldsymbol{\Sigma}\cdot\boldsymbol{m} = \psi(\boldsymbol{\varepsilon})\boldsymbol{I}\cdot\boldsymbol{m} - (\partial\boldsymbol{u}/\partial\boldsymbol{x})^{\top}\underbrace{\boldsymbol{\sigma}\cdot\boldsymbol{m}}_{=\boldsymbol{0}} = \psi(\boldsymbol{\varepsilon})\cdot\boldsymbol{m}. \tag{19}$$

Ignoring the line integral term of (18) assumes that ψ is continuous across the crack edges and results in (17) being domain size dependent when ψ is not continuous across the crack edges, whereas (18) is always domain independent.

It is important here to clarify the difference between the nodal CF in the context of finite element configurational force mechanics, and the CF at the crack tip. The CF at the crack tip is $\boldsymbol{G}$ (15); (17) and (18) are only representations of $\boldsymbol{G}$. The nodal CF values for any element in the finite element mesh are given by

$$\{\boldsymbol{g}\} = \int_K [\boldsymbol{B_I}]^{\top}\{\boldsymbol{\Sigma}\}d\mathbf{x}, \tag{20}$$

where $\boldsymbol{g}$ is a vector containing the nodal CF values for K. Unless specified otherwise, CF refers to $\boldsymbol{G}$, and its finite element representations (17) and (18), not the nodal CF values $\{\boldsymbol{g}\}$. For an isotropic homogeneous material acting in plane stress both components of the $\boldsymbol{G}$ can be described using stress intensity factors

$$\boldsymbol{G} = \frac{1}{E}\begin{Bmatrix}K_{\mathrm{I}}^2 + K_{\mathrm{II}}^2\\ -2K_{\mathrm{I}}K_{\mathrm{II}}\end{Bmatrix}, \tag{21}$$

where K_{I} and K_{II} are the mode I and mode II stress intensity factors respectively, and E is Young's modulus. For homogeneous linear elastic materials K_I and K_{II} can be determined from $\boldsymbol{G}$, with the local FE displacement field. Alternatively in the case of anisotropic materials, where the relationship between $\boldsymbol{G}$ and the SIFs is more complex, a Newton method can be used, [12]. However, both these methods require knowledge of the local stress field.

3.2. Reliability of error estimator for the Configurational force

Up to an arbitrary constant C_η, η has been shown in [7] to bound the true error of the solution in the DG norm (9). In this section, a proof showing that the area integral in (17) and (18) can be bound by η up to an arbitrary constant is provided. In order to show that the error estimate is reliable for error in the area integral contribution (17) and (18), some definitions are required. Firstly, the L^2 norm of all elements K in the mesh $\mathcal{T}$

$$\| * \|_{0,\mathcal{T}} = \left(\sum_{K\in\mathcal{T}} \| * \|^2_{0,K(\mathcal{T})} \right)^{1/2} = \left(\sum_{K\in\mathcal{T}} \int_K | * |^2 d\mathbf{x} \right)^{1/2}$$

additionally from the definition of infinitesimal strain

$$\begin{aligned} \|\boldsymbol{\varepsilon}\|_{0,\mathcal{T}} &= \|(\boldsymbol{h} + \boldsymbol{h}^\top)/2\|_{0,\mathcal{T}} \\ &\leq (\|\boldsymbol{h}\|_{0,\mathcal{T}} + \|\boldsymbol{h}\|_{0,\mathcal{T}})/2 = \|\boldsymbol{h}\|_{0,\mathcal{T}}, \quad \text{where} \quad \boldsymbol{h} = \nabla \boldsymbol{u}_h \end{aligned} \tag{22}$$

For the material stiffness matrix there exist the constant $D_{\max} = \max_{i,j,k,l\in[1,2]}(D_{ijkl})$, such that

$$\begin{aligned} \|\boldsymbol{\sigma}\|_{0,\mathcal{T}} &= \|\boldsymbol{D} : \boldsymbol{\varepsilon}\|_{0,\mathcal{T}} \\ &\leq D_{\max}\|\boldsymbol{\varepsilon}\|_{0,\mathcal{T}} \\ &\leq D_{\max}\|\boldsymbol{h}\|_{0,\mathcal{T}} \end{aligned} \tag{23}$$

Using (22) and (23) it can be shown that $\boldsymbol{\Sigma}$ is bound by $\boldsymbol{h}$, that is

$$\begin{aligned} \|\Sigma\|_{0,\mathcal{T}} &= \|\psi\mathbf{I} - \boldsymbol{h}^\top\boldsymbol{\sigma}\|_{0,\mathcal{T}} \\ &\leq \|\psi\|_{0,\mathcal{T}} + \|\boldsymbol{h}^\top\boldsymbol{\sigma}\|_{0,\mathcal{T}} = \|\boldsymbol{\sigma} : \boldsymbol{\varepsilon}\|_{0,\mathcal{T}}/2 + \|\boldsymbol{h}^\top\boldsymbol{\sigma}\|_{0,\mathcal{T}} \\ &\leq \|\boldsymbol{\sigma}\|_{0,\mathcal{T}}\|\boldsymbol{\varepsilon}\|_{0,\mathcal{T}}/2 + \|\boldsymbol{h}\|_{0,\mathcal{T}}\|\boldsymbol{\sigma}\|_{0,\mathcal{T}} \\ &\leq 3/2\|\boldsymbol{\sigma}\|_{0,\mathcal{T}}\|\boldsymbol{h}\|_{0,\mathcal{T}} \\ &\leq 3/2 D_{\max}\|\boldsymbol{h}\|^2_{0,\mathcal{T}}. \end{aligned}$$

Since $\|\boldsymbol{h} - \boldsymbol{h}_h\|_{0,\mathcal{T}}$ is a component of $|||\boldsymbol{u} - \boldsymbol{u}_h|||_{\mathcal{T}}$, and using the reliability result from [7], $|||\boldsymbol{u} - \boldsymbol{u}_h|||_{\mathcal{T}} \leq C_\eta\eta$, it is possible to write,

$$\|\Sigma - \Sigma_h\|_{0,\mathcal{T}} \leq 3/2 D_{\max}\|\boldsymbol{h} - \boldsymbol{h}_h\|^2_{0,\mathcal{T}} \leq C_\Sigma\eta^2 \tag{24}$$

where C_Σ is a positive constant independent of the size and polynomial order of the elements in the mesh and the magnitude of the load applied on the boundary, and the subscript h denoting the finite element approximated value of a variable. Next we introduce the function $\boldsymbol{V} \in \mathscr{B}_\Gamma \to \mathbb{R}^2$, which is representative of the summation operators in (17) and (18). The function $\boldsymbol{V}$ acts as a virtual displacement, each component of $\boldsymbol{V}$ varies continuously from 1 at the crack tip, to 0 at the boundary $\partial\mathscr{B}$. This allows the norm of the area integral of (18) to written with the following result,

$$\|\nabla\boldsymbol{V} : \Sigma - \nabla\boldsymbol{V} : \Sigma_h\|_{0,\mathcal{T}} \leq \|\nabla\boldsymbol{V}\|_{0,\mathcal{T}}\|\Sigma - \Sigma_h\|_{0,\mathcal{T}} \leq C_\Sigma\|\nabla\boldsymbol{V}\|_{0,\mathcal{T}}\eta^2 \tag{25}$$

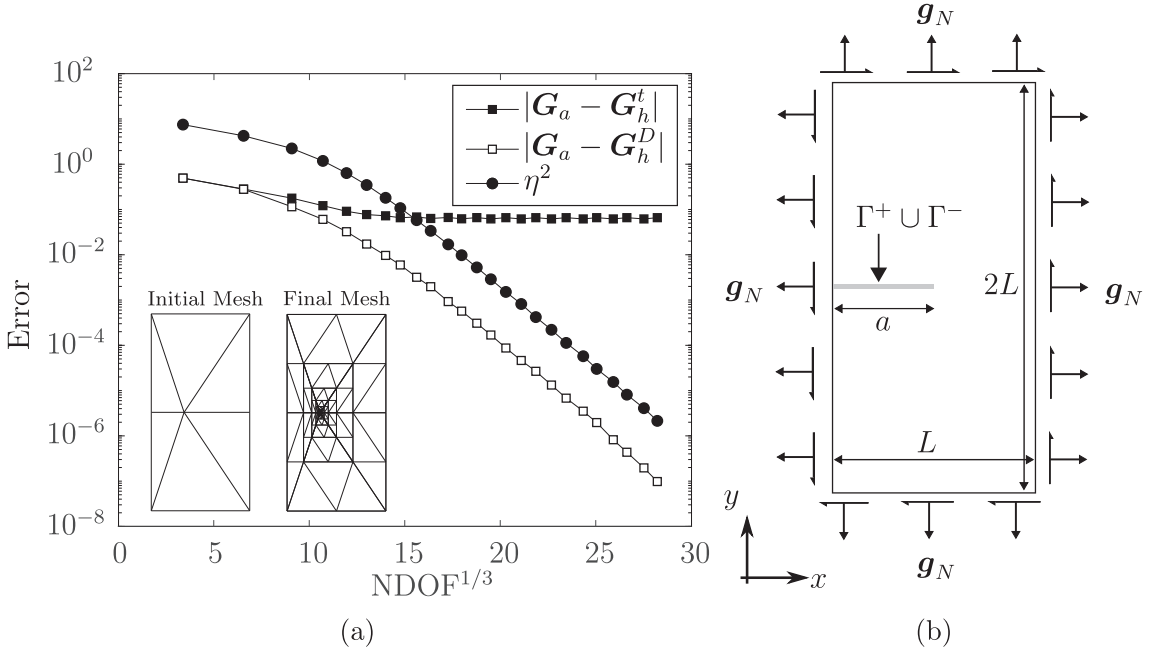

Fig. 2. Westergaard crack in an infinite plate: (a) CF error for the domain and tip methods (17), and the value of error estimate squared against NDOF$^{1/3}$, with the initial mesh before refinement and final mesh after refinement shown by the inset figures. (b) Geometry of the truncated Westergaard problem, with the crack edges shown by the greyed line.

where $\|\nabla \boldsymbol{V}\|$ is independent of the mesh and the elements used. Since η is always known and (25) shows that the error in the area integral of (18) will converge at the same rate, η^2 provides a measure of the total improvement to the area integral of (18). When considering a problem with a single crack the area component of (17) and the integral (18) are considered over the whole problem domain. However when a problem contains multiple crack tips, the CF calculations (17) and (18) are considered on a subdomain of the mesh $\mathcal{T}^c \subset \mathcal{T}$ about the crack tip. Therefore when quantifying the error in the CF calculation for a crack tip, the same subdomain used to calculate $\boldsymbol{G}_h$ is used to determine the error estimate. The error estimate value computed over the subdomain is denoted η^c and gives a sharper bound to (25) for a crack tip, where $\eta^c \in \bar{\eta}^c$ with $\bar{\eta}^c$ as the set of the error estimate values considered on all separate element sets about each crack tip.

3.3. Convergence of the CF error with the error estimate

The Westergaard mixed mode crack problem is used here to show numerically the efficacy of using a *hp*-adaptive method driven by an error estimate to achieve very high accuracies of the CF using the domain method $\boldsymbol{G}_h^D$. Further the problem is used to demonstrate the lack of convergence in the CF error when only considering the nodal CF value at the crack tip node $\boldsymbol{G}_h^t$. However, the Westergaard problem is not general since ψ is continuous across the crack edges. As such the analytical solution of (17) is equal to (18) as the line integral terms of (18) are zero. For a more general problem the issue of domain dependence of (17) is discussed and the necessity, and difficulty, of including the line integral terms in (18) is explored.

3.3.1. Westergaard problem

The geometry of the truncated domain of the Westergaard mixed mode problem and boundary conditions are shown in Fig. 2(b) with $L = 1$ m and the crack length $a = 0.5$ m. The stress solution of the infinite plate is applied as a Neumann boundary condition to the edges of the truncated domain as

$$\boldsymbol{g}_N = \begin{Bmatrix} \sigma_{xx}\cdot \boldsymbol{n}_x + \sigma_{xy}\cdot \boldsymbol{n}_y \\ \sigma_{xy}\cdot \boldsymbol{n}_x + \sigma_{yy}\cdot \boldsymbol{n}_y \end{Bmatrix}, \quad \text{where} \quad \partial\mathscr{B}_N = \partial\mathscr{B} \backslash \left(\Gamma^+ \cup \Gamma^- \right), \tag{26}$$

where σ_{xx}, σ_{yy} and σ_{xy} are the infinite plate stress solutions from [82]. The normal and shear stress at infinity are $\sigma_\infty = \tau_\infty = 1$ Pa, the plate acts in plane stress with a Young's modulus of $E = 5/2$ Pa, and a Poisson's ratio $\nu = 0.3$. Since no Dirichlet boundary conditions are applied to this problem, the problem is made determinant by applying average boundary conditions to restrain rigid body motion, as in [6]. The analytical solution of the CF values for the Westergaard problem is determined from the relationship between the CF at the crack tip and the stress intensity factors for the problem using (21), where $K_I = \sigma_\infty \sqrt{\pi a}$ and $K_{II} = \tau_\infty \sqrt{\pi a}$. The initial mesh for the Westergaard problem is shown in Fig. 2(a) with $p_K = 3 \; \forall \; K \in \mathcal{T}$. 25 *hp*-adaptive steps were applied to the mesh with the constants $\delta_2 = 0.3$ and $\delta_1 = 0.07$ for Algorithm 1, this produced the final mesh also shown in the inset figures in Fig. 2(a). $\boldsymbol{G}$ is determined by $\boldsymbol{G}_h^D$ and $\boldsymbol{G}_h^t$ from (17), where the domain size of $\boldsymbol{G}_h^D$ is kept constant and is defined by the elements of the initial mesh which share a node at the crack tip, in this case all 6 elements of the mesh.

Fig. 2(a) shows that $\boldsymbol{G}_h^D$ converges exponentially with the cubed root of the number of degrees of freedom (NDOF$^{1/3}$) with a *hp*-adaptive scheme driven by an error estimator. After 25 refinement steps an absolute error of 9.716×10^{-8} ($\approx 5.7 \times 10^{-6}$% error) is achieved, at least 4 orders of magnitude greater in accuracy than [14]. $\boldsymbol{G}_h^D$ converges at the same rate as η^2 which is consistent with (25).

Although an initial improvement in the calculation of $\boldsymbol{G}_h^t$ is seen in the first 7–8 adaptivity steps, the solution plateaus to an

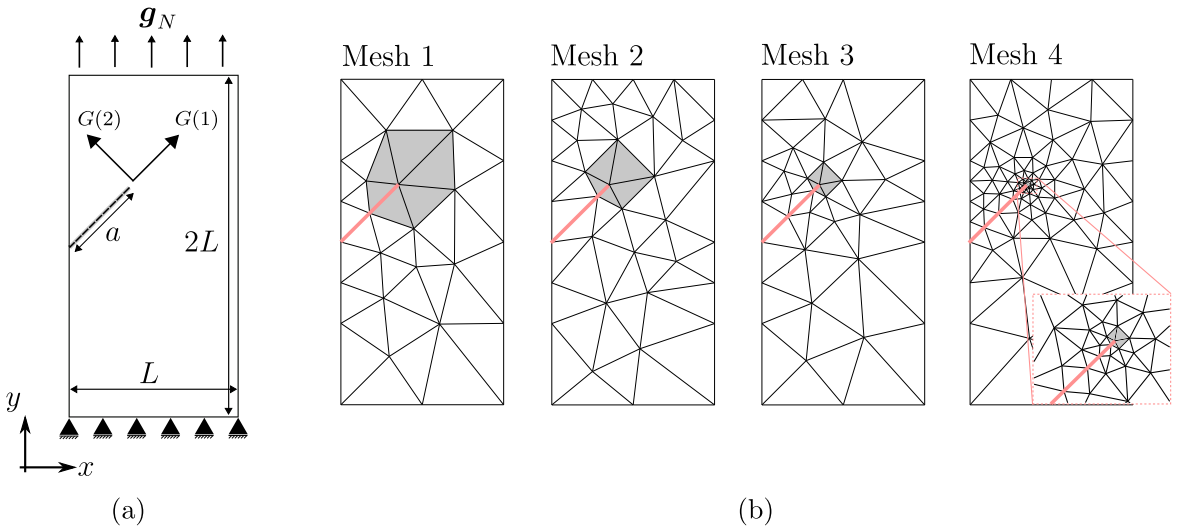

Fig. 3. Inclined edge crack: (a) geometry of the slanted crack problem with initial meshes 1, 2, 3 and 4 shown in (b).

absolute error of $\approx 10^{-1}$. The plateau is caused by the strongest part of the singularity which resides in the elements that have a node on the crack tip. A finite element that has an arbitrarily high polynomial basis is unable to describe well a singular function. This error is seen clearly when calculating $\boldsymbol{G}_h^t$ for the Westergaard problem. $\boldsymbol{G}_h^t$ is domain independent so acts like a normalised stress error of the elements at the crack tip. However, when considering $\boldsymbol{G}_h^D$ and performing a *hp*-adaptive refinement, the crack tip elements, which are unable to model the singularity, become smaller exponentially fast. The result is their contribution to $\boldsymbol{G}_h^D$, and therefore also their associated error, decreases and so continued exponential convergence of $\boldsymbol{G}_h^D$ to the analytical solution of $\boldsymbol{G}$ is achieved.

3.3.2. Inclined edge crack

An inclined edge crack problem, Fig. 3(a), is presented here to demonstrate the domain dependence of $\boldsymbol{G}_h^D$ (17). Specifically the component of $\boldsymbol{G}_h^D$ that acts perpendicular to the crack edges for a straight crack. The plate acts in plane stress with $E = 5/2$ Pa, $\nu = 0.3$, $L = 1$ m, an inclined crack set at 45° to the horizontal with length $a = \sqrt{2}/4$ m, a homogeneous Dirichlet boundary condition is applied on the bottom most edge, a normal traction $\boldsymbol{g}_N = [01]^\top$ Pa on the top edge and a homogeneous Neumann boundary condition on all remaining edges.

Four initial meshes are consider with $p_K = 3 \; \forall \; K \in \mathcal{T}$, as shown in Fig. 3(b). The domain size for the calculation of $\boldsymbol{G}_h^D$ for each mesh is determined by the elements at the crack tip for each initial mesh, marked by the grey regions in Fig. 3(b). For meshes 1–4 the radius of the domain size is approximately 0.17868 m, 0.0707 m, 0.0354 m, 0.0035 m, respectively. Last, 30 *hp*-adaptive steps, from Algorithm 1, were applied to the problem with $\delta_2 = 0.3$ and $\delta_1 = 0.07$. The results of the parallel, $G_h^D(1)$, and perpendicular, $G_h^D(2)$, components of $\boldsymbol{G}_h^D$ to the crack edges are shown in Fig. 4(a). The parallel components converge to a value invariant of the domain size, whereas the perpendicular components are a function of the domain size.

The domain dependence is caused by the non-zero nodal CF values on the crack edges which act perpendicular to crack edges, unlike the internal nodal CF values which do tend to zero. This is expressed clearly in Fig. 4(b) where the norm of the nodal CF values acting perpendicular to the crack edge, $|g(2)|$ of $\boldsymbol{g}$, for every node along the crack edge (excluding the crack tip node) is plotted against the node's distance away from the crack tip. For a node, $|g(2)|$ is calculated using all elements that contain that node, this includes element either side of the crack edge. Fig. 4(b) shows that $|g(2)|$ has non-zero values at nodes along the crack edge for refinement steps 5, 10 and 15 of mesh 4, hence increasing the domain size of $\boldsymbol{G}_h^D$ will consider more non-zero nodal CF values along the crack edges, unlike the interior nodes which are zero (excluding the crack tip node).

This can be explained in the context of CF mechanics by considering four elements of a mesh $\mathcal{T}_K = \{K_1, K_2, K_3, K_4\} \subset \mathcal{T}$ and their edges $\mathcal{F}_K = \{F_1, F_2, F_3, F_4, F_5, F_6, F_7, F_8\} \subset \mathcal{F}$, as shown in Fig. 5. The configurational velocity $\boldsymbol{V}$ is a test function for the nodal value of $\{\boldsymbol{g}\}$ on the white filled node in Fig. 5. $\boldsymbol{V}$ varies continuously from 1 on the white filled node to 0 on the black filled node. Two types of edges are present, crack edges marked in grey, $\{F_1, F_2\}$, and internal edges marked in black, $\{F_3, F_4, F_5, F_6, F_7, F_8\}$. The Eshelby stress $\boldsymbol{\Sigma}$ is assumed to vary continuously across the internal edges with jumps in its value existing between the crack edges, this is assumed to demonstrate that even if the $\boldsymbol{\Sigma}$ is continuous across elements in the mesh, nodal CF values will still exist along the crack edges. Last, since the material is homogeneous $\nabla\boldsymbol{\Sigma} = \boldsymbol{0}$.

Starting with integration by parts of $\boldsymbol{\Sigma}$: $(\nabla \boldsymbol{V})$ for an element K

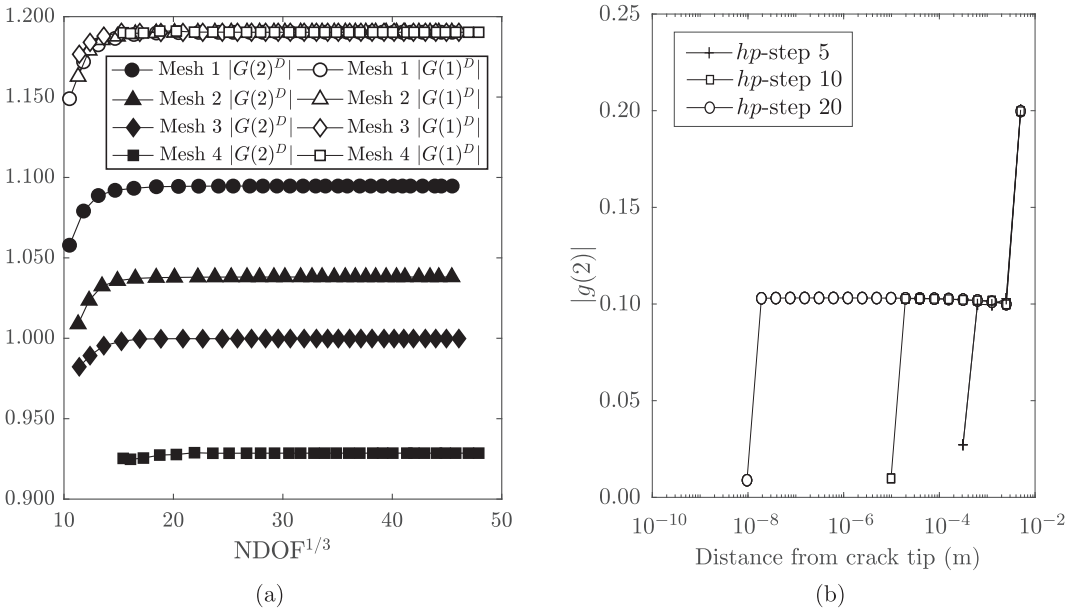

Fig. 4. Inclined edge crack: (a) $|G_h^D(1)|$ and $|G_h^D(2)|$ for the inclined crack problem. (b) The absolute perpendicular value of $\boldsymbol{g}$, $|g(2)|$, for each node along the crack edges for mesh 4.

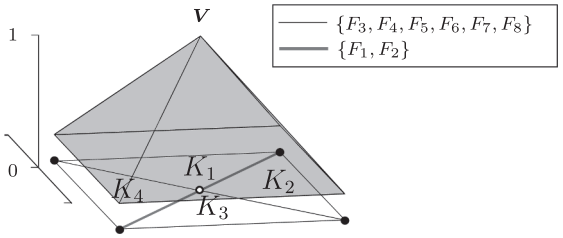

Fig. 5. A subsection of the mesh $\mathcal{T}_K = \{K_1, K_2, K_3, K_4\} \subset \mathcal{T}$ with the continuous variation of $\boldsymbol{V}$, shown by the grey triangle, from 1 on the white filled node to 0 on the boundary nodes, marked in black.

$$\int_K \boldsymbol{\Sigma}\!:\!\Big(\nabla \boldsymbol{V}\Big) d\mathbf{x} = \int_K \Big(\nabla\cdot\boldsymbol{\Sigma}\Big)\cdot\boldsymbol{V} d\mathbf{x} - \int_K \nabla\cdot\Big(\boldsymbol{\Sigma}\cdot\boldsymbol{V}\Big) d\mathbf{x}, \tag{27}$$

and as $\nabla\boldsymbol{\Sigma} = \boldsymbol{0}$

$$\int_K \boldsymbol{\Sigma}\!:\!\Big(\nabla \boldsymbol{V}\Big) d\mathbf{x} = -\int_K \nabla\cdot\Big(\boldsymbol{\Sigma}\cdot\boldsymbol{V}\Big) d\mathbf{x}. \tag{28}$$

Using the Gauss-Green theorem (28) becomes

$$\int_K \boldsymbol{\Sigma}\!:\!\Big(\nabla \boldsymbol{V}\Big) d\mathbf{x} = -\int_{\partial K} \mathbf{n}\cdot\Big(\boldsymbol{\Sigma}\cdot\boldsymbol{V}\Big) ds, \tag{29}$$

and summing together the contribution from all four elements gives

$$\sum_{K\in\mathcal{T}_K} \int_K \boldsymbol{\Sigma} : (\nabla \boldsymbol{V}) d\mathbf{x} = -\sum_{F\in\mathcal{F}_K} \int_F [\![\boldsymbol{\Sigma}\cdot\boldsymbol{V}]\!] ds \tag{30}$$

As $\boldsymbol{V}$ and $\boldsymbol{\Sigma}$ are continuous across all $F \in \mathcal{F}_K$, but not necessarily across the crack edges, only the line integral along the element edges which coincides with the crack edges is non-zero

$$\sum_{K\in\mathcal{T}_K} \int_K \boldsymbol{\Sigma} : (\nabla \boldsymbol{V}) d\mathbf{x} = -\int_{F_1\cup F_2} [\![\boldsymbol{\Sigma}\cdot\boldsymbol{V}]\!] ds \tag{31}$$

Rewriting $\boldsymbol{V}$ and $\nabla\boldsymbol{V}$ in terms of a vector nodal constants $\{\boldsymbol{V}_I\}$ for element K with corresponding shape functions and shape function derivatives, $[\boldsymbol{N}_I]\{\boldsymbol{V}_I\}$ and $[\boldsymbol{B}_I]\{\boldsymbol{V}_I\}$ respectively, (31) can written using matrix notation as

$$\sum_{K\in\mathcal{T}_K} \int_K \{\boldsymbol{V}_I\}^\top [\boldsymbol{B}]_I^\top \{\Sigma\} d\mathbf{x} = -\int_{F_1\cup F_2} [\![\{\boldsymbol{V}_I\}^\top [\boldsymbol{N}_I]^\top \{\Sigma\}]\!] ds \tag{32}$$

As $\{\boldsymbol{V}_I\}$ is a vector of constants it can be removed from both sides of the equation leaving

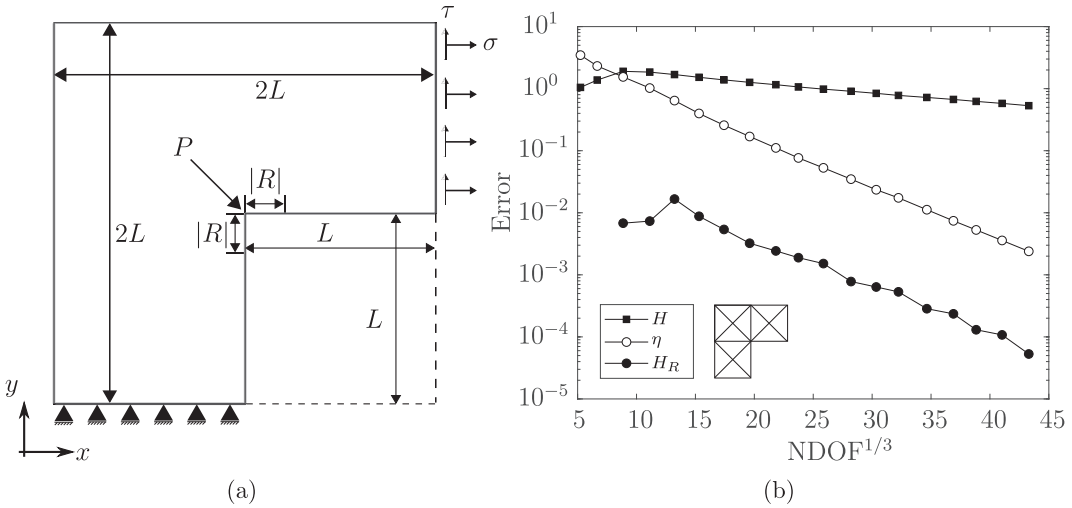

Fig. 6. (a) The geometry of the L-shaped. (b) Convergence plots of η, H and H_R with *hp*-adaptive refinement against the NDOF$^{1/3}$ for the L-shaped domain. The initial mesh for the L shaped domain is inset in (b).

$$\{\boldsymbol{g}_I\} = \sum_{K\in\mathcal{T}_K}\int_K [\boldsymbol{B}]_I^\top\{\boldsymbol{\Sigma}\}d\mathbf{x} = -\int_{F_1\cup F_2}[\![[\boldsymbol{N}_I]^\top\{\boldsymbol{\Sigma}\}]\!]ds \tag{33}$$

where $\{\boldsymbol{g}_I\}$ is a vector containing the CF nodal values in x and y for all $K\in\mathcal{T}_K$ which, since $\boldsymbol{\Sigma}$ is not continuous across the crack edges, has non-zero values for all the nodes along the crack edges, agreeing with Fig. 4(b). The result is that by increasing the domain size more non-zero values of $\{\boldsymbol{g}\}$ along the crack edges are included in the calculation of the CF, the CF value therefore will converge to a different value depending on the domain size.

3.3.3. Line integrals near singularities

In order to use the domain independent CF calculation, (18), a line integral along the crack edges is required. However as highlighted by [17,60], amongst others, there are difficulties associated with trying to evaluate the crack edge term of (18).

For a crack in an isotropic homogeneous plate it is well known that the displacement field near a crack tip is $\boldsymbol{u}\propto r^{1/2}$, where r is the distance away from the crack tip, [34]. Investigating the Sobolev space of the displacement field shows that in the interior of the domain $\boldsymbol{u}\in[H^{3/2-\epsilon}]^2$ [76]. The Sobolev space on the boundary of the domain can be measured using a trace inequality, it is found that the displacement field along a crack edge near the crack tip is in $[H^{1-\epsilon}]^2$ [63], where ϵ is small number. Therefore since stress is a function of the differential of displacement the stress field on the same boundary is $\boldsymbol{\sigma}\in[H^{-\epsilon}]^{3\times3}$ and therefore not quite in the L^2 norm. The stress field on the boundary next to the crack tip is therefore unable to be modelled by a finite element approximation with a polynomial basis. Hence integrating along the crack edge to the determine the CF will lead to poor results. However, this is not unique to crack problems, but occurs more generally when a stress singularity exists along a boundary. In this case, dependent on the strength of the singularity, the $L2$ norm of the error in the stress field along the boundary does not converge, or at best, converges very slowly.

Consider the problem presented by Fig. 6(a); a L-shaped domain with side length $L=1$ m. A Neumann boundary condition is applied on the far right edge with $\mathbf{g}_N=[11]^\top$ Pa, a homogeneous Dirichlet boundary condition is applied to the bottom most edge and homogeneous Neumann boundary conditions are applied everywhere else. The initial mesh is shown by the inset figure in Fig. 6(b) and has $p_K=3\ \forall\ K\in\mathcal{T}$, the mesh undergoes *hp*-adaptivity with the constants $\delta_2=0.3$ and $\delta_1=0.07$.

At point P a stress singularity exists with the attached edges having homogeneous Neumann boundary conditions applied. As in [7], the results in Fig. 6(b) show that η converges exponentially with NDOF$^{1/3}$. Fig. 6(b) also shows that the error in the $L2$ norm of tractions along the homogeneous Neumann boundary $\partial\mathscr{B}_{NO}\subset\partial\mathscr{B}_N$

$$H=\sqrt{\int_{\partial\mathscr{B}_{N0}}\left|\boldsymbol{\sigma}_h\cdot\mathbf{n}\right|^2},$$

converges at a rate much slower than η. However if the $L2$ norm error calculation is performed along $\partial\mathscr{B}_{NO}\backslash R$, that is excluding the region R of length $|R|$

$$H_R=\sqrt{\int_{\partial\mathscr{B}_{N0}\backslash R}\left|\boldsymbol{\sigma}_h\cdot\mathbf{n}\right|^2},$$

where R is of arbitrary length, but is set as $|R|=0.05$ m, but includes the point P, convergence of a rate similar to η is achieved as the singular part of the function is not included in the error calculation.

4. A general domain independent method for G

In Section 3.3.2 the issue of domain dependence has been highlighted for $G_h^D(2)$ for problems where the jump in energy across the crack edges is not zero. In order to compute $\boldsymbol{G}$, whilst not making assumptions of the stress field around the crack tip, a line integral is required along the crack edges. But as shown in Section 3.3.3, the convergence of the error of a stress field along edges is poor when a singularity exists on the edges, therefore a new method to overcome this difficulty is required in which exponential convergence is obtained with *hp*-adaptivity.

The new method considers (18) but excludes a region R on the crack edges that contains the crack tip such that $\boldsymbol{G}_h^\Gamma$ is redefined as

$$\boldsymbol{G}_h^{\Gamma\backslash R}=-\sum_{K\in A}\sum_{n_K\in n_b}\int_K[\boldsymbol{B}_I]^\top\{\boldsymbol{\Sigma}\}d\mathbf{x}+\sum_{(\partial K\in(\Gamma^+\cup\Gamma^-)\backslash R)}\sum_{n_K\in n_b}\int_{\partial K}[\boldsymbol{N}_I]^\top\left\{\psi(\boldsymbol{\varepsilon})\cdot\boldsymbol{m}\right\}ds+\sum_{\Gamma\in\{\Gamma^+,\Gamma^-\}}\left\{\left|R\right|\times\max_{\Gamma\backslash R}\left[\psi(\boldsymbol{\varepsilon})\right]\right\}\cdot\boldsymbol{m}, \tag{34}$$

where the crack edges, $(\Gamma^+\cup\Gamma^-)$, consider all of the crack edges up to the node at the crack tip. The last component of (34) is adding the maximum energy along a crack edge multiplied by the length $|R|$, where R corresponds to the excluded region of a single crack edge. This is included as the stress field cannot be evaluated along the crack edges next to the crack tip, instead it is assumed that the stress field will increase but at unknown rate. Therefore the maximum energy is including to approximate the length of the crack edge that is not included.

By excluding an arbitrary region R along a line that contains a singularity, exponential convergence of the error in the stress field along the line is obtained as this portion of the boundary has a regular stress field. However, for the computation of $\boldsymbol{G}$ the region R is by definition 0, and therefore not arbitrary. In order to achieve accurate results the proposed method has to ensure that the stress solution along $\Gamma^+\cup\Gamma^-\backslash R$ improves and that $|R|\to0$. The *hp*-adaptive scheme, Algorithm 1, improves the stress solution along $\Gamma^+\cup\Gamma^-\backslash R$. R is reduced such that the number of elements considered with R always increases, *h*-refinement will normally occur at the crack tip as this is where the highest errors exist. This ensures that in the finite element solution the singularity becomes more

localised to the crack tip and the effect of the singularity on the calculation of $\Gamma^+ \cup \Gamma^- \backslash R$ reduces i.e. the regularity of the element in R which is also adjacent to $\Gamma^+ \cup \Gamma^- \backslash R$ increases and thus the effect of the singularity on the error of the calculation along $\Gamma^+ \cup \Gamma^- \backslash R$ reduces.

Consider Fig. 7, at refinement step 0 six elements are considered within O, with the region R being the same as region $\Gamma^+ \cup \Gamma^-$. The length of the crack edges excluded by R for the initial mesh is l m. From the initial mesh to refinement step 1 an *hp*-adaptive step has occurred, increasing the number of elements from six to 24. However the region R is not reduced by an element edge length since the number of elements within R will not increase. Only once a second *hp*-refinement step has occurred to produce step 2 does R reduce as the number of element edges considered within R increases from 1 in the initial mesh, to 2 in refinement step 2. This pattern is summarised in Table 1. By reducing R in this fashion ensures that the size of R will go to zero. The size of the element edge length at the crack tip is always reducing by half, therefore $|R| \rightarrow 0$ is defined by the following series,

$$\left| R \right| = l - \sum_{q=1}^{\infty} \frac{l}{2q} = 0. \tag{35}$$

where q is a count of every other *hp*-adaptive step (assuming h refinement at the crack).

4.1. Mixed mode Westergaard problem

In Section 3.3.3 it was shown that the error in the homogeneous Neumann boundary condition converged at a similar rate to the error estimate if the component along the boundary containing the singularity was ignored. In this section the efficacy of the method presented in Section 4 to evaluate the energy along the crack edges for the CF calculation, (18) is measured using the Westergaard problem. The same material properties, boundary conditions, initial mesh and *hp*-refinement strategy (running for 35 *hp*-refinement steps) as in Section 3.3.1 for the mixed mode Westergaard problem was considered. The $L2$ norm of all three stress components along the crack edges is analysed using,

$$E_m = \lim_{|R|\rightarrow 0} \left(\left\| \boldsymbol{\sigma}_h - \boldsymbol{\sigma}_W \right\|^2_{0,(\Gamma^+ \cup \Gamma^-)\backslash R} \right) \tag{36}$$

where $m = [1, 2]$ and defines E_m for crack edge 1, $m = 1$, or crack edge 2, $m = 2$. E_m also bounds the equivalent error in the energy along the crack edges as $\|\psi(\boldsymbol{\varepsilon})\| \lesssim \|\boldsymbol{\sigma}\|^2$

$$\lim_{|R|\rightarrow 0} \left(\|\psi(\boldsymbol{\varepsilon})_h - \psi(\boldsymbol{\varepsilon})_W\|_{0,(\Gamma^+ \cup \Gamma^-)\backslash R} \right) \lesssim \lim_{|R|\rightarrow 0} \left(\left\| \boldsymbol{\sigma}_h - \boldsymbol{\sigma}_W \right\|^2_{0,(\Gamma^+ \cup \Gamma^-)\backslash R} \right), \tag{37}$$

where $\psi(\boldsymbol{\varepsilon})$ is the Westergaard solution for the elastic strain energy.

The length of R is decreased by the strategy described in Section 3.3.3, the exponential convergence of $|R| \rightarrow 0$ with $\text{NDOF}^{1/3}$ is shown in Fig. 8(a) and the convergence in the error measure $E_1 + E_2$ is shown in Fig. 8(b). The oscillations in $E_1 + E_2$ are caused by the change in the size of R acting to increase the error, whilst the refinement occurring along $\Gamma^+ \cup \Gamma^- \backslash R$ act to reduce the error. Overall the convergence of $|\boldsymbol{G} - \boldsymbol{G}_h^{\Gamma \backslash R}|$ is similar to that of η, therefore for problems without an analytical solution the convergence of η is used as an indicator to the convergence of the $G^{\Gamma \backslash R}(2)$. The minimum value for the error measure $|\boldsymbol{G} - \boldsymbol{G}_h^{\Gamma \backslash R}|$ is $\approx 5 \times 10^{-}7$, at least 10^4 smaller than the error achieved by Denzer et al. [14], an alternative method which makes no assumption about the local stress field but one which also incorrectly assumes the energy contribution from the crack faces is zero. A highlight of this method is its simplicity, the authors appreciate that a goal-orientated error estimate for the edge term of (34) could be used to as an error measure for the CF however this would require an adjoint problem to be solved at each iteration step; detracting from overall simplicity of this algorithm.

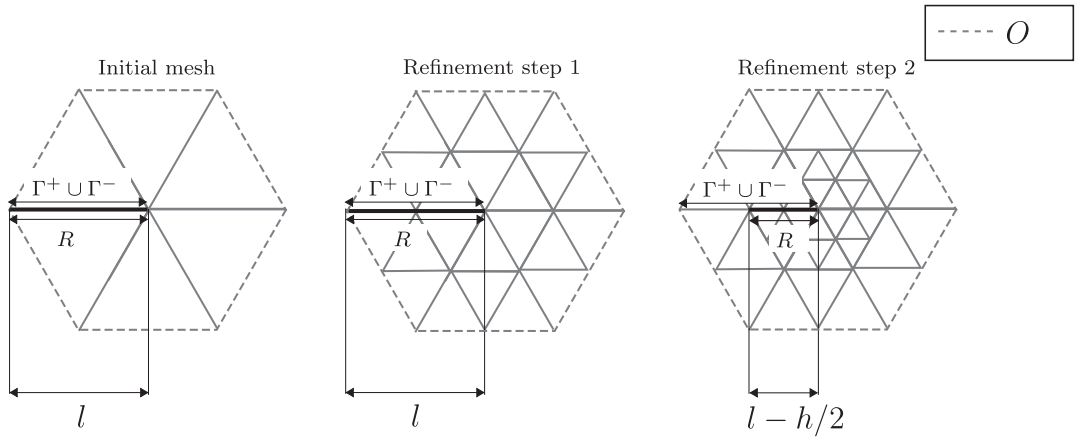

Fig. 7. The first 2 refinement steps and the corresponding reduction in the excluded length adjacent to the crack tip, R.

Table 1
How the number of edges considered inside R and the total corresponding length excluded from (34) varies with refinement steps.

Refinement step	Number of edges excluded	Size of R
0	1	l
1	1	l
2	2	$l - l/2$
3	2	$l - l/2$
4	3	$l - l/2 - l/4$
5	3	$l - l/2 - l/4$

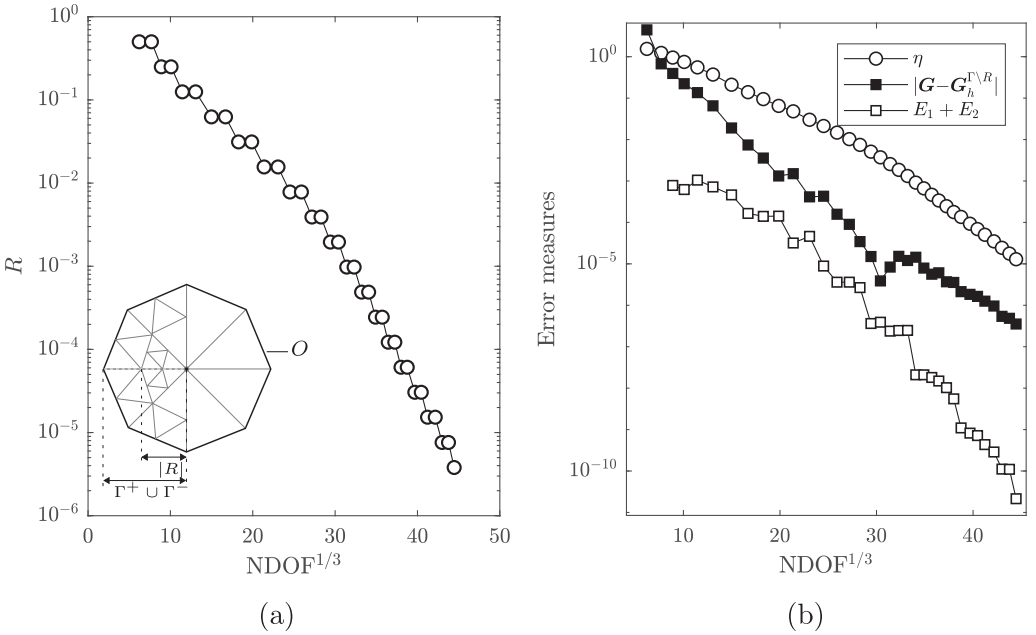

Fig. 8. Westergaard crack in an infinite plate: (a) excluded length $|R|$ with NDOF$^{1/3}$ and (b) error measures against NDOF$^{1/3}$.

5. Numerical examples

Combining the error estimate (11), the *hp*-adaptive strategy, Algorithm 1, and $\boldsymbol{G}_h^{\Gamma\setminus R}$, it was shown that very accurate results in comparison to an analytical solution of $\boldsymbol{G}$ were possible for the area integral component of (18) in Section 3.3.1 and the line integral component of (18) in Section 4.1.

For straight cracks the parallel component of $G_h^{\Gamma\setminus R}(1)$ is bound by η^2 up to an arbitrary positive constant. The error in $G_h^{\Gamma\setminus R}(2)$ for the increasing domain size was shown numerically to converge at similar rate as η whilst the domain size not included in the line integral, R, decreased exponentially to 0. Since the error estimate is not strictly greater than the error in $\boldsymbol{G}_h^{\Gamma\setminus R}$, the exact accuracy of $\boldsymbol{G}_h^{\Gamma\setminus R}$ cannot be stated. Instead we present $G_h^{\Gamma\setminus R}(1)$ and $G_h^{\Gamma\setminus R}(2)$ with the number of significant figures that η^2 and η have reduced by; based on the assumption that the orders of magnitude for $G_h^{\Gamma\setminus R}(1)$ and $G_h^{\Gamma\setminus R}(2)$ do not change. All problems are plates acting in plane stress with $E = 5/2$ Pa, $\nu = 0.3$ with $p_K = 3\forall\ K \in \mathcal{T}$ and with a limit is set on p_K of 10. The limit on p_K was applied to prevent very high order elements appearing the mesh. Although exponential convergence is maintained using continually higher orders with the current *hp* marking scheme, the marking scheme does suffer in this instance from continually marking elements for *p*-refinement even if the error of the element is negligible. The result is the solver time becomes large and with negligible reduction in the size η. By limiting the polynomial order the solver time is decreased and the rate of convergence is also increased. Finally, all initial meshes were generated using Triangle [36].

5.1. Inclined edge crack

The first problem to be investigated is the inclined edge crack problem, visited in Section 3.3.2. This problem is used to demonstrate that the convergence of $\boldsymbol{G}_h^{\Gamma\setminus R}$ is domain independent. For the purpose of readability the problem is redefined as an inclined crack in a finite plate, Fig. 3(a), with a traction of $\boldsymbol{g}_N = [01]^\top$ Pa acting on the top boundary and with a fixed homogeneous Dirichlet boundary on the bottom edge. The *hp*-adaptivity strategy used $\delta_2 = 0.3$ and $\delta_1 = 0.07$ and ran for 30 adaptive steps. The initial and final meshes are shown in Figs. 3(b) and 9 respectively.

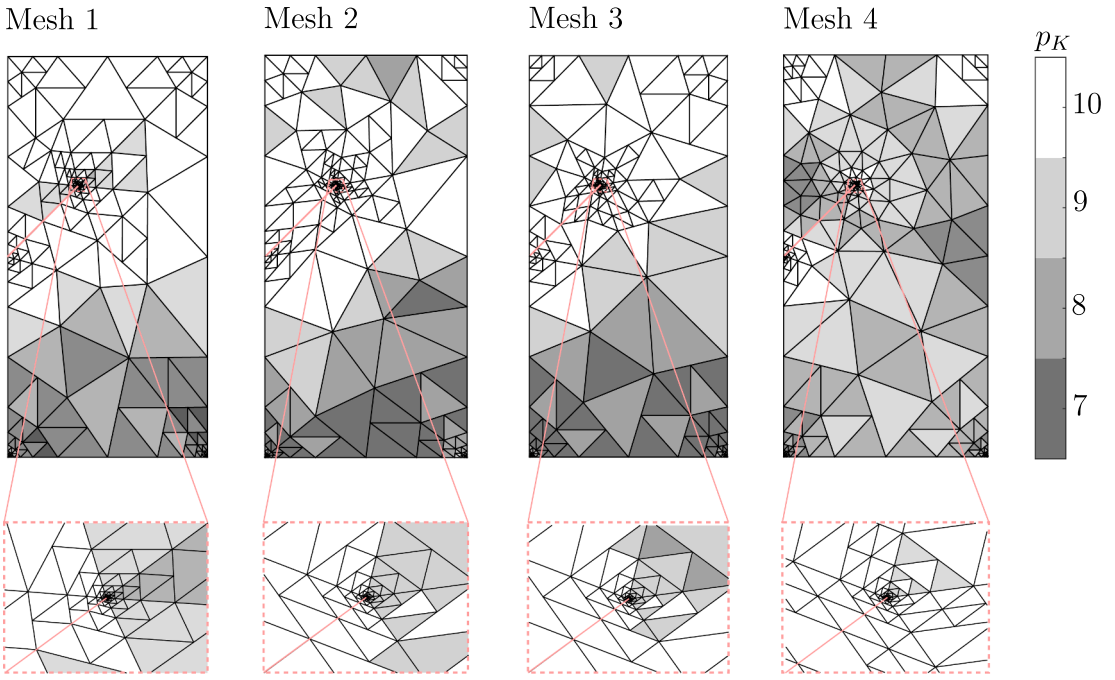

Fig. 9. Inclined edge crack: The final element and polynomial distribution for meshes 1–4 after 30 *hp*-refinement steps with an enlarged view of the elements about the crack tip.

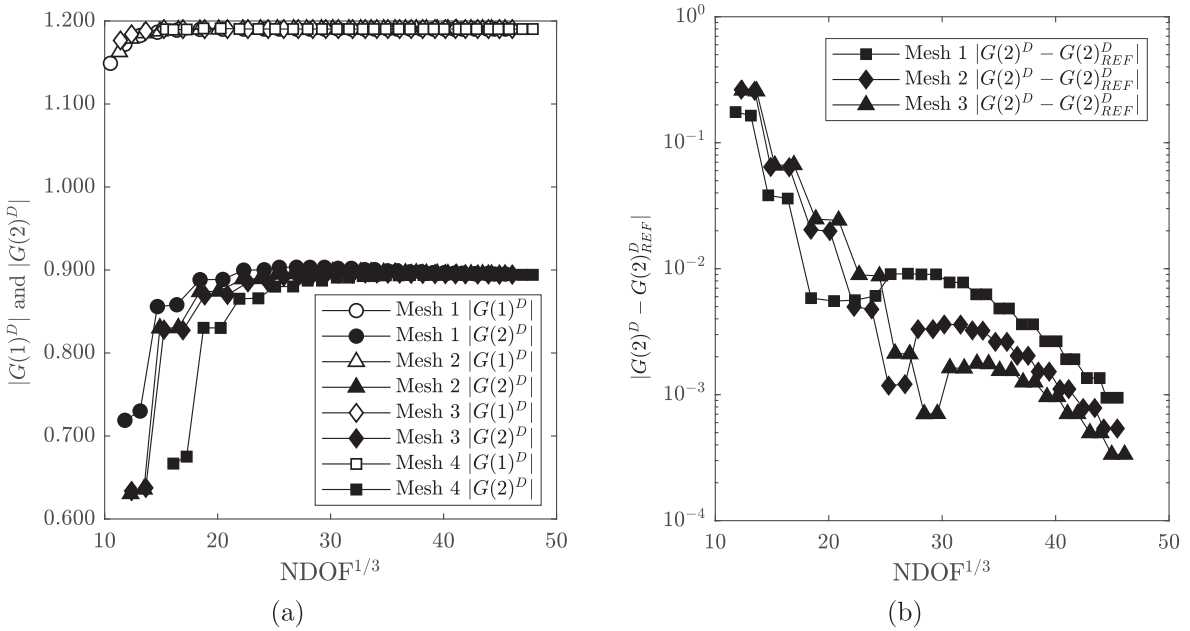

Fig. 10. Inclined crack: (a) convergence of $|G_h^D(1)|$ and $|G_h^D(2)|$ for meshes 1–4 and (b) the convergence of $|G_h^D(2)|$ for meshes 1–3 compared to the final value of $|G_h^D(2)|$ for mesh 4.

Table 2
Inclined edge crack: $\boldsymbol{G}_h^{\Gamma\backslash R}$ values acting perpendicular and parallel to the crack edges.

	Mesh 1	Mesh 2	Mesh 3	Mesh 4
$G_h^{\Gamma\backslash R}(1)$	1.1902868	1.1902868	1.1902868	1.1902868
$G_h^{\Gamma\backslash R}(2)$	−0.8951	−0.8947	−0.8945	−0.8942

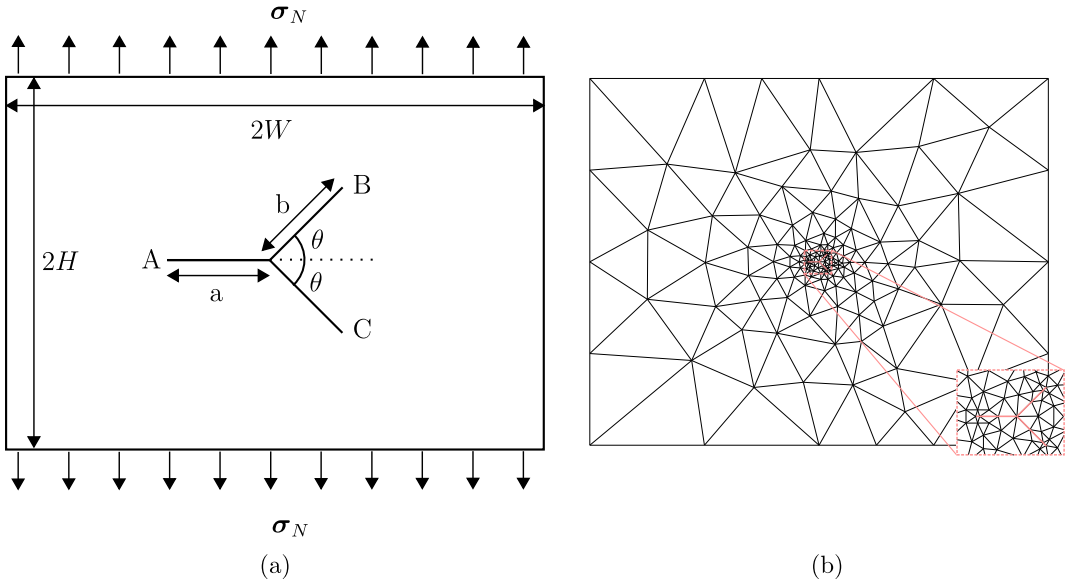

Fig. 11. Split crack: (a) the geometry and loading conditions with the initial mesh with $p_K = 3 \forall\ K \in \mathcal{T}$ shown in (b).

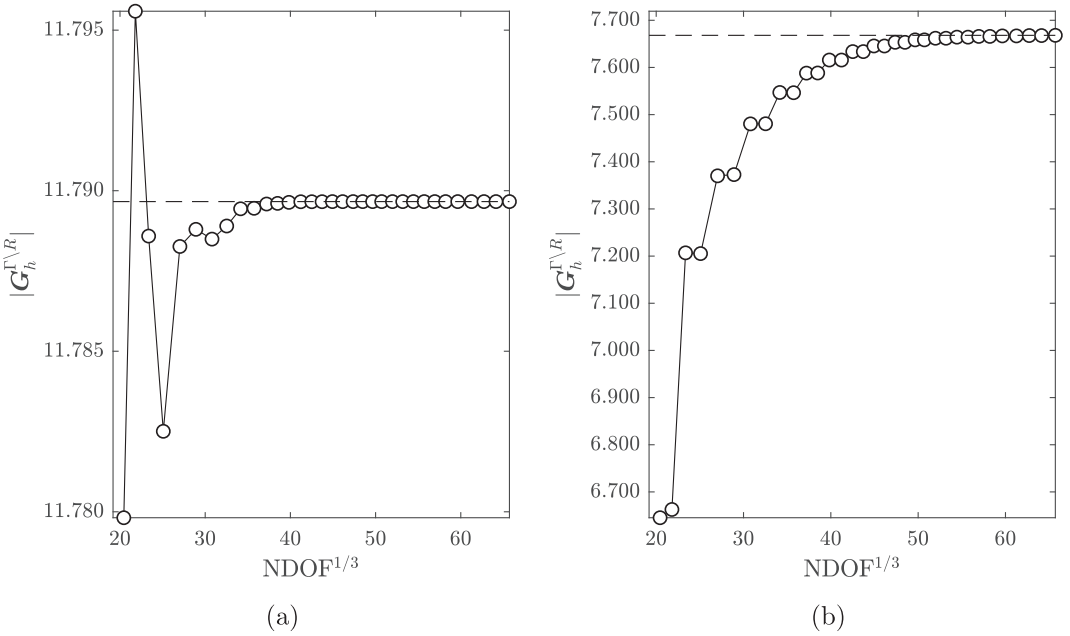

Fig. 12. Split crack: (a) $\boldsymbol{G}_h^{\Gamma\backslash R}$ for crack A and (b) $\boldsymbol{G}_h^{\Gamma\backslash R}$ for crack B/C. The final converged value for both plots is indicated by the dashed line.

Four different meshes where used, as shown in Fig. 3(b), each with a different domain size which is highlighted in grey on each initial mesh. The convergence of $G_h^{\Gamma\backslash R}(1)$ and $G_h^{\Gamma\backslash R}(2)$ for each different domain size is shown in Fig. 10(a). The figure shows for all domain sizes $G_h^{\Gamma\backslash R}(2)$ converges to the same value. Since $G_h^{\Gamma\backslash R}(1)$ is bound by η^2 faster convergence is observed, whereas $G_h^{\Gamma\backslash R}(2)$, which was demonstrated to converge at a similar rate to η, converged slower. The final values for $G_h^{\Gamma\backslash R}(1)$ and $G_h^{\Gamma\backslash R}(2)$ are given in Table 2. By considering the final value of $G_h^{\Gamma\backslash R}(2)$ for mesh 4 as a reference solution, Fig. 10(b) demonstrates exponential convergence of $G^{\Gamma\backslash R}(2)$ towards the same value for all four domain sizes.

Similar to Fig. 8(b), Fig. 10(a) shows a staircase like convergence for the perpendicular value of $\boldsymbol{G}_h^{\Gamma\backslash R}$. To give the improvement of the parallel and perpendicular components of $\boldsymbol{G}_h^{\Gamma\backslash R}$ the error estimator η_c is calculated for the domain used to calculate $\boldsymbol{G}_h^{\Gamma\backslash R}$. Overall η_c decreased by a factor of $\approx 2 \times 10^4$ for all meshes, indicating a decrease in the error for the perpendicular component of $\approx 2 \times 10^4$ and a giving a minimum decrease of the parallel component of $\approx 4 \times 10^8$.

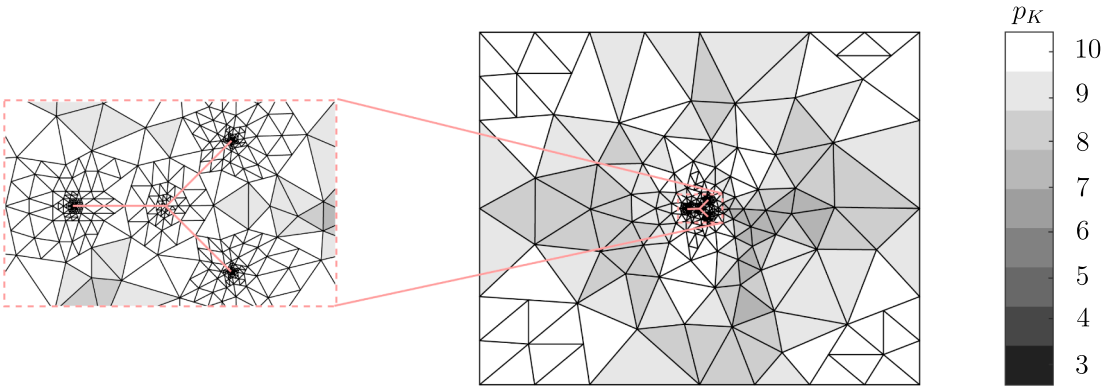

Fig. 13. A colour plot of the final element distribution and polynomial order after 35 refinement steps. (For interpretation of the references to colour in this figure legend, the reader is referred to the web version of this article.)

Table 3
Split crack: the final values of $G_h^{\Gamma\setminus R}(1)$ and $G_h^{\Gamma\setminus R}(2)$ for cracks A, B and C (as shown in Fig. 11(a)).

	$G_h(1)$ [77]	$G_h^{\Gamma\setminus R}(1)$	$G_h(2)$ [77]	$G_h^{\Gamma\setminus R}(2)$	$\lvert \boldsymbol{G}_h \rvert$ [77]	$\lvert \boldsymbol{G}_h^{\Gamma\setminus R} \rvert$
A	11.691	11.789604	0	$-18.943634 \times 10^{-11}$	11.691	11.789604
B	5.396	5.424	5.396	5.417	7.630	7.666
C	5.396	5.424	−5.396	−5.417	7.630	7.666

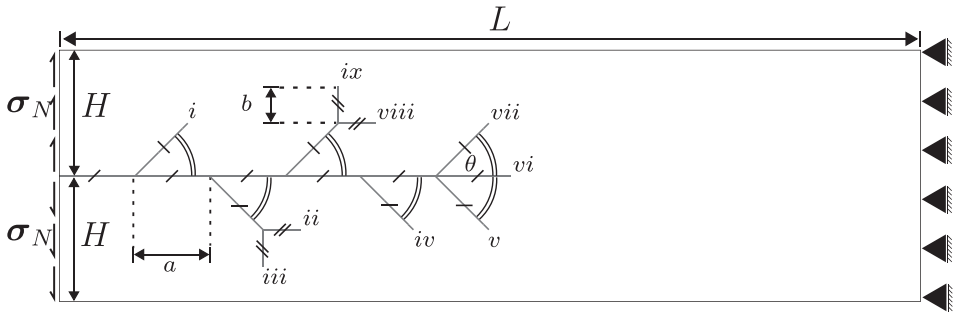

Fig. 14. Tree crack: geometry, loading conditions and boundary conditions.

5.2. Split crack

The split crack problem, Fig. 11(a), has been visited in literature by [77,10], amongst others. In this section a comparison is made between the CF obtained from the stress intensity factors from [77] against the values achieved by $\boldsymbol{G}_h^{\Gamma\setminus R}$. The stress intensity factors in [77] were obtained using an enrichment function in conjunction with the interaction integral [83] where the crack is straight and where the shape of the stress field at the crack tip has to be known *a priori*. The geometry, and corresponding initial mesh, of the problem is shown in Fig. 11(a) and (b) respectively.

The dimensions and loads applied to the split crack problem are, $H = 16$ m, $W = 20$ m, $a = b = 1$ m, and $\boldsymbol{\sigma}_N = [00.2]^\top$ MPa applying a uniaxial tension to the plate. As no Dirichlet boundary conditions exist, average boundary conditions are applied for the vertical displacement and rotation to restrict rigid body motion, [6]. The *hp*-adaptive strategy ran for 35 refinement steps using $\delta_2 = 0.3$ and $\delta_1 = 0.07$ with the initial and final mesh shown in Figs. 11(b) and 13.

As $\lvert \boldsymbol{G}_h \rvert$ is of a similar order of magnitude for each crack, the crack tip singularity is near the same strength for each crack. η_K^2 for the elements at all the crack tips is therefore a similar magnitude, resulting in 32 *h*-refinements for elements at the cracks B and C and 34 *h*-refinements for the elements at crack A. The *hp*-strategy is therefore effective at identifying multiple singular regions in the mesh, at each crack tip only *h*-refinement has occurred meaning an efficient adaptive strategy has been performed, since these regions are singular, as well as meaning the calculation of $\boldsymbol{G}_h^{\Gamma\setminus R}$ can occur whilst $|R| \to 0$. The convergence of $\lvert \boldsymbol{G}_h^{\Gamma\setminus R} \rvert$ for crack A is shown in Fig. 12(a), and the convergence of $\lvert \boldsymbol{G}_h^{\Gamma\setminus R} \rvert$ for cracks B and C is shown in Fig. 12(b).

The normalised value of $\boldsymbol{G}_h^{\Gamma\setminus R}$ is displayed on Fig. 12(a) for crack A, and Fig. 12(b) for cracks B and C. Since the refinement for cracks B and C was nearly symmetric the results of $\boldsymbol{G}_h^{\Gamma\setminus R}$ were indistinguishable and so plotted as the same line. The final values for the components of $G_h^{\Gamma\setminus R}(1)$ and $G_h^{\Gamma\setminus R}(2)$ for each crack are given in Table 3. The results obtained here are in excellent agreement with

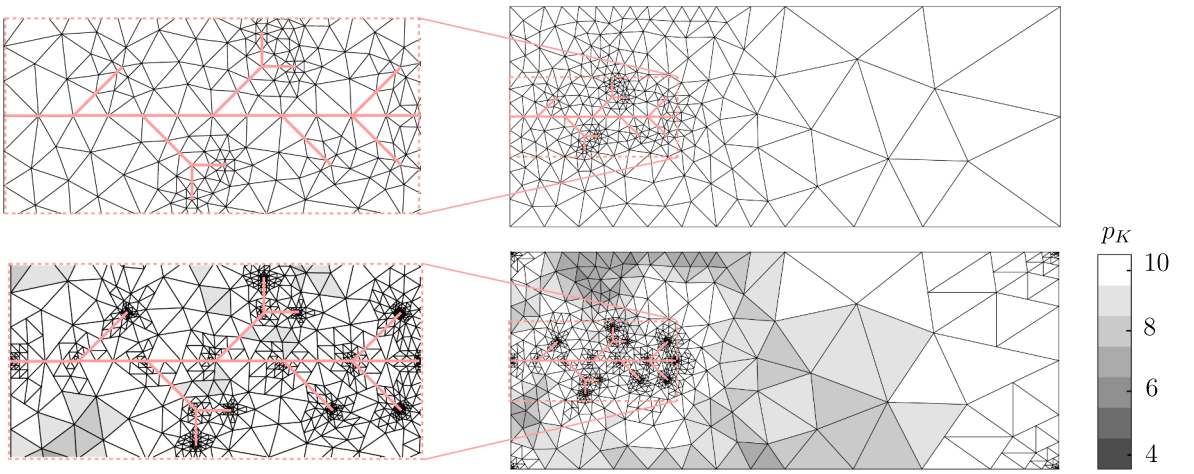

Fig. 15. Tree crack: top right is the initial mesh of the whole problem, with an expanded view of the mesh about the cracks on the top left. Bottom right is a colour plot of the element polynomial and element distribution of the final mesh after 35 *hp*-adaptive steps with an expanded view of the mesh about the cracks on the bottom left. (For interpretation of the references to colour in this figure legend, the reader is referred to the web version of this article.)

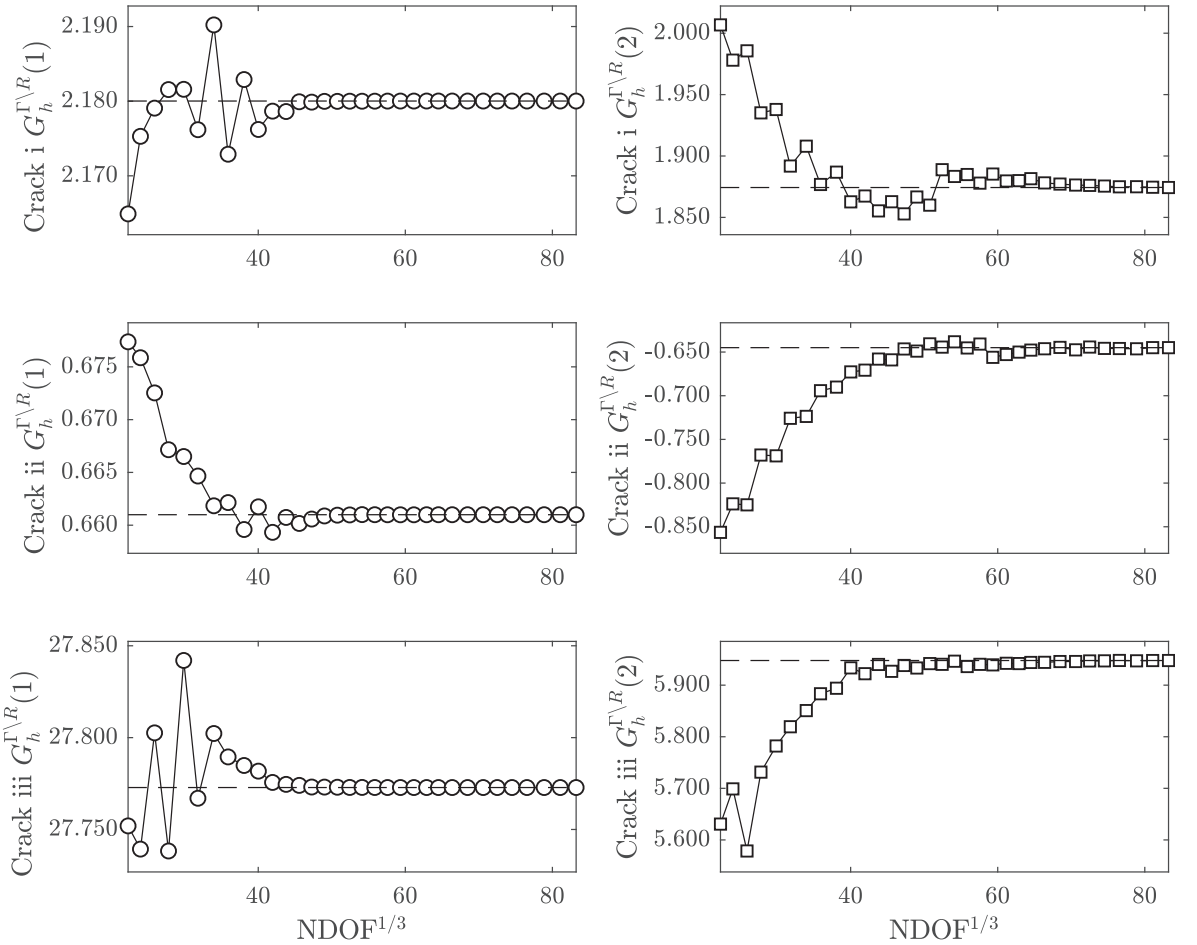

Fig. 16. Tree crack: $G_h^{\Gamma\backslash R}(1)$ and: $G_h^{\Gamma\backslash R}(2)$ for cracks *i* to *iii*.

[77]. Both $G_h^{\Gamma\backslash R}(1)$ and $G_h^{\Gamma\backslash R}(2)$ converge to a value slightly above that found by [77] suggesting that the results obtained in [77] have not sufficiently converged. The calculation of $\boldsymbol{G}_h^{\Gamma\backslash R}$ for each crack only occurs on a portion of the mesh. Therefore η^c is used to determine the overall accuracy of the calculation of $\boldsymbol{G}_h^{\Gamma\backslash R}$ for each individual crack. Overall η^c changes by a magnitude ranging from

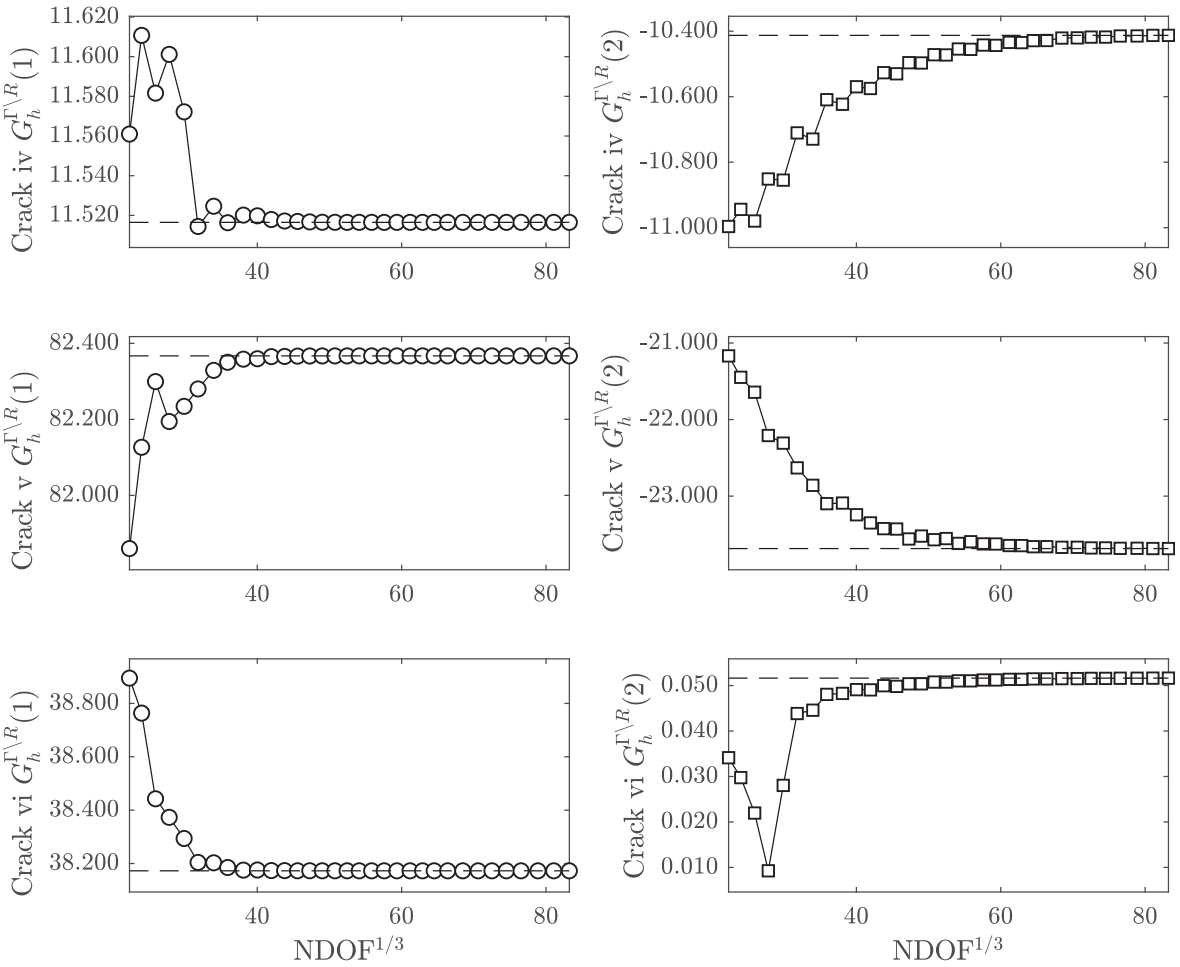

Fig. 17. Tree crack: $G_h^{\Gamma\backslash R}(1)$ and: $G_h^{\Gamma\backslash R}(2)$ for cracks *iv* to *vi*.

4.5×10^4 to 5.6×10^4, and $(\eta^c)^2$ changed by a magnitude ranging from 5.8×10^9 to 3.4×10^9.

5.3. Tree crack

The final problem considered is the tree-crack problem, previously visited by Ai et al. [2]. The geometry and loading conditions are shown in Fig. 14 with outer dimensions $L = 20$ m and $H = 4$ m. A slight variant of this problem was considered by [2,46] where the tree crack geometry was contained within a square which had a biaxial tensile load applied. However that problem contains closing cracks which neither [2] or [46] consider producing unusable results. The tree crack is marked by the grey lines with dimensions $a = 1$ m, $b = 0.5$ m and $\theta = \pi/4$. A traction of $\mathbf{g}_N = [01]^\top$ Pa was applied on the left most edge acting to open up the crack edges and a weak homogeneous Dirichlet boundary condition applied on the right most edge. The adaptivity strategy uses $\delta_2 = 0.3$ and $\delta_1 = 0.07$, with a limit set on p_K of 10, and ran for 35 refinement steps with $p_K = 3 \; \forall \; K \in \mathcal{T}$ for the initial mesh, shown in Fig. 15. The problem contains 9 opening cracks and so at each crack tip a singular stress field exists of relatively different strengths. The convergence of the $G_h^{\Gamma\backslash R}(1)$ and $G_h^{\Gamma\backslash R}(2)$ for the 9 cracks are shown in Figs. 16–18. As the *hp*-adaptive algorithm refines the mesh, the level of *hp*-refinement that occurs at each step about each crack tip will be relatively larger or smaller than a neighbouring crack tip. During the initial stages of the *hp*-adaptivity the value of $\boldsymbol{G}_h^{\Gamma\backslash R}$ at a crack tip was significantly affected by the *hp*-adaptivity occurring by nearby surround crack tips. Despite 9 cracks in the problem the adaptivity method picks up all cracks, Fig. 15. A maximum of 34 *h*-refinement steps occurs for the elements at crack *vi* whilst a minimum of 28 *h*-refinement steps occurs at crack *ii*. In order to compute $\boldsymbol{G}_h^{\Gamma\backslash R}$, *h*-adaptivity about the crack tip in order for $|R| \to 0$ is required. The tree-crack problem therefore shows that even for a problem considering multiple crack tips of different strengths, the combined error estimate, *hp*-adaptivity and $\boldsymbol{G}_h^{\Gamma\backslash R}$ is effective at computing accurate results for $\boldsymbol{G}$.

For this more complex problem the same pattern of convergence for the parallel and perpendicular components of $\boldsymbol{G}_h^{\Gamma\backslash R}$ is observed. For all 9 cracks fast convergence of $G_h^{\Gamma\backslash R}(1)$ is observed as the total error for all 9 cracks is bound by η^2. Whereas $G_h^{\Gamma\backslash R}(2)$ converges more slowly as it was shown to converge at the same rate as η. Additionally it was noted for such a complex problem

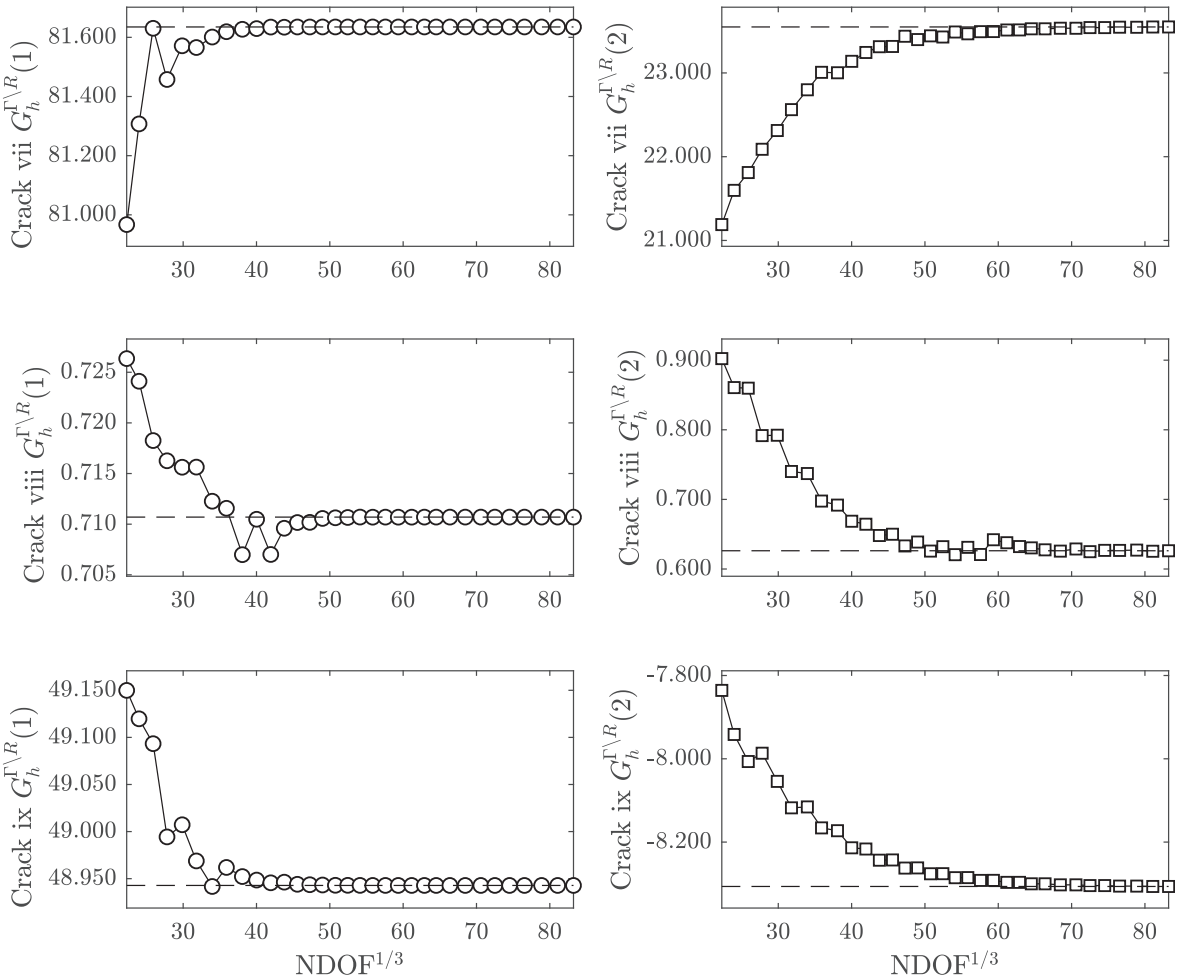

Fig. 18. Tree crack: $G_h^{\Gamma\setminus R}(1)$ and: $G_h^{\Gamma\setminus R}(2)$ for cracks *vii* to *ix*.

Table 4
Tree crack: a comparison between $\boldsymbol{G}_h^{\Gamma\setminus R}$ and equivalent G values obtained using the stress intensity factors from [2].

Crack number	$G_h^{\Gamma\setminus R}(1)$	$G_h(1)$ [2]	$G_h^{\Gamma\setminus R}(2)$	$G_h(2)$ [2]
i	2.18002	2.54	1.87	2.14
ii	0.660993	0.803	− 0.646	− 0.718
iii	27.7728	–	5.94	–
iv	11.5165	–	− 10.4	–
v	82.367037	–	− 23.69	–
vi	38.172645	35.3	0.05167	0
vii	81.635063	–	23.55	–
viii	0.71070	–	0.626	–
ix	48.942	48.6	− 8.308	− 8.10

communication occurring between cracks with *hp*-refinement. For instance no *hp*-refinement or change in R could occur around a crack tip, however refinement about another crack tip could cause the value of $\boldsymbol{G}_h^{\Gamma\setminus R}$ to change.

Similar to the split crack problem, the calculation of $\boldsymbol{G}_h^{\Gamma\setminus R}$ for each crack only occurred on a portion of the mesh. Therefore η^c is used to determine the overall accuracy of the calculation of $\boldsymbol{G}_h^{\Gamma\setminus R}$ for each individual crack. Overall η_c changed by a maximum magnitude of 4×10^4 for crack *vi* and a minimum magnitude of 3×10^3 for crack *ii*. The final values of the stress intensity values and their corresponding values of $\boldsymbol{G}_h^{\Gamma\setminus R}$ are given in Table 4. The results agree fairly well with the available values provided by [2]. Significantly less refinement was performed by [2] and the direction of the convergence was not always clear, it is therefore considered that the results presented here are a new benchmark.

6. Conclusion

This paper proposed a novel method to determine the CF at the crack tip which does that not require knowledge of the stress field about the crack tip to be known *a priori*. The error of the crack tip CF component that acted parallel to the crack edges was shown to be bound by η^2, where as the error of the component which acted perpendicular to the crack tip demonstrated convergence at a similar rate to η. Since η converges exponentially this enabled where accurate benchmarks for the CF value acting parallel and perpendicular to the crack edges can be produced; providing benchmarks for the inclined, split and tree crack problem. Additionally for the split and tree crack problem the CF agreed excellently with the results available in the literature. Assuming that the value of the CF computed for the initial mesh was of the same magnitude of the final mesh, the accuracy of both values of the CF can be given to the correct number of significant figures. Overall the method presents itself as a way to directly compute the CF accurately, this opens the door to a method where the CF can be used for fatigue analysis for homogeneous isotropic materials as well highly accurate crack propagation. Further, with a minimal modification of the error estimator, the method could be used to determine the CF directly for both heterogeneous, anisotropic and combined heterogeneous and anisotropic materials where determining the near crack tip stress solution is not trivial.

The main difficulty associated with calculating the CF is determining the CF component that acts perpendicular to the crack face. The perpendicular component requires integrals along the crack faces which are difficult to evaluate. The CF components that act in plane with the crack face only require domain integrals. In two dimensions the face contribution to the perpendicular CF is calculated by ignoring an increasing larger number of element edges at the crack tip, with the total length of the ignored element edges made increasingly smaller. For the three dimensional case the two inplane components of the CF are evaluated with only a domain integral, but similar to two dimensions, the perpendicular component requires integrals along the crack faces. Therefore a similar methodology to the one presented here could be applied to a three dimensional case, but instead of ignoring element edges at the crack tip element faces are ignored at the crack front. For a more detailed description of evaluating CFs on three dimensional crack fronts, albeit only using domain integrals, see the work of Kaczmarczyk et al. [37].

It was also demonstrated and discussed how considering the nodal CF component at the crack tip will lead to results of poor accuracy, and how domain methods which only consider area integrals to determine the CF at the crack can only be applied to a small range of problems. Finally an investigation and explanation as to why integrating the stress field along a crack edge will result in a poor solution is presented.

Acknowledgements

This work was supported by the Engineering and Physical Sciences Research Council [grant number EP/M507854/1]. The authors acknowledge the support of the European Commission-funded RISE-project BESTOFRAC (734370). All data produced in this paper is available at doi:https://doi.org/10.15128/r270795766r.

References

[1] Adams T, Giani S, Coombs WM. A high-order elliptic PDE based level set reinitialisation method using a discontinuous Galerkin discretisation. J Comput Phys 2019;379:373–91.
[2] Ai W, Augarde CE. A multi-cracked particle method for complex fracture problems in 2D. Math Comput Simul 2018;150:1–24.
[3] Alatawi IA, Trevelyan J. A direct evaluation of stress intensity factors using the extended dual boundary element method. Eng Anal Bound Elem 2015;52:56–63.
[4] Barsoum RS. Triangular quarter-point elements as elastic and perfectly-plastic crack tip elements. Int J Numer Meth Eng 1977;11(1):85–98.
[5] Belytschko T, Black T. Elastic crack growth in finite elements with minimal remeshing. Int J Numer Meth Eng 1999;45(5):601–20.
[6] Bird R, Coombs WM, Giani S. A quasi-static discontinuous Galerkin configurational force crack propagation method for brittle materials. Int J Numer Meth Eng 2017;113(7):1061–80.
[7] Bird R, Coombs WM, Giani S. A posteriori discontinuous Galerkin error estimator for linear elasticity. Appl Math Comput 2019(344):78–96. Awaiting publication.
[8] Bordas S, Duflot M. Derivative recovery and a posteriori error estimate for extended finite elements. Comput Meth Appl Mech Eng 2007;196(35):3381–99.
[9] Braun M. Configurational forces induced by finite element discretization. Proc Eston Acad Sci, Ser Phys Math 1997;46(1/2):24–31.
[10] Chen YZ, Hasebe N. New integration scheme for the branch crack problem. Eng Fract Mech 1995;52(5):791–801.
[11] Cho JR, Lee HW. Calculation of stress intensity factors in 2-D linear fracture mechanics by Petrov-Galerkin natural element method. Int J Numer Meth Eng 2014;98(11):819–39.
[12] Chu SJ, Hong CS. Application of the Jk integral to mixed mode crack problems for anisotropic composite laminates. Eng Fract Mech 1990;35(6):1093–103.
[13] Cirak F, Ekkehard R. A posteriori error estimation and adaptivity for linear elasticity using the reciprocal theorem. Comput Meth Appl Mech Eng 1998;156(1):351–62.
[14] Denzer R, Barth FJ, Steinmann P. Studies in elastic fracture mechanics based on the material force method. Int J Numer Meth Eng 2003;58(12):1817–35.
[15] Duflot M, Bordas S. A posteriori error estimation for extended finite elements by an extended global recovery. Int J Numer Meth Eng 2008;76(8):1123–38.
[16] Eibner T, Melenk JM. An adaptive strategy for hp-FEM based on testing for analyticity. Comput Mech 2007;39(5):575–95.
[17] Eischen JW. An improved method for computing the J2 integral. Eng Fract Mech 1987;26(5):691–700.
[18] Ern A, Stephansen AF, Zunino P. A discontinuous Galerkin method with weighted averages for advection-diffusion equations with locally small and anisotropic diffusivity. IMA J Numer Anal 2009;29(2):235–56.
[19] Ern A, Stephansen AF, Vohralík M. Guaranteed and robust discontinuous Galerkin a posteriori error estimates for convection-diffusion-reaction problems. J Comput Appl Math 2010;234(1):114–30.
[20] Eshelby JD. The force on an elastic singularity. Philos Trans Roy Soc A 1951;224(877):87–112.
[21] Eshelby JD. Energy relations and the energy-momentum tensor in continuum mechanics. Fundamental contributions to the continuum theory of evolving phase interfaces in solids: a collection of reprints of 14 seminal papers. Berlin, Heidelberg: Springer; 1999. p. 82–119.
[22] Fagerström M, Larsson R. Theory and numerics for finite deformation fracture modelling using strong discontinuities. Int J Numer Meth Eng 2006;66(6):911–48.
[23] Fawkes AJ, Owen DRJ, Luxmoore AR. An assessment of crack tip singularity models for use with isoparametric elements. Eng Fract Mech 1979;11(1):143–59.
[24] González-Estrada OA, Nadal E, Ródenas JJ, Kerfriden P, Bordas S, Fuenmayor FJ. Mesh adaptivity driven by goal-oriented locally equilibrated superconvergent patch recovery. Comput Mech 2014;53(5):957–76.
[25] Griffith AA. VI.The phenomena of rupture and flow in solids. Philos Trans Roy Soc Lond A: Math Phys Eng Sci 1921;221(582–593):163–98.
[26] Gurtin ME. Configurational forces as basic concepts of continuum physiscs. New York: Springer-Verlag; 2000.
[27] Gurtin ME, Podio-Guidugli P. Configurational forces and the basic laws for crack propagation. J Mech Phys Solids 1996;44:905–27.

[28] Hansbo P, Larson MG. Energy norm a posteriori error estimates for discontinuous Galerkin approximations of the linear elasticity problem. Comput Meth Appl Mech Eng 2011;200(45):3026–30.
[29] Hattori G, Alatawi IA, Trevelyan J. An extended boundary element method formulation for the direct calculation of the stress intensity factors in fully anisotropic materials. Int J Numer Meth Eng 2017;109(7):965–81.
[30] Heintz P, Larsson F, Hansbo P, Runesson K. Adaptive strategies and error control for computing material forces in fracture mechanics. Int J Numer Meth Eng 2004;60(7):1287–99.
[31] Hellen TK. On the method of virtual crack extensions. Int J Numer Meth Eng 1975;9(1):187–207.
[32] Heuer ME, Mellado N, Stephan EP. *hp*-adaptive two-level methods for boundary integral equations on curves. Computing 2001;67(4):305–34.
[33] Houston P, Robson J, Süli E. Discontinuous Galerkin finite element approximation of quasilinear elliptic boundary value problems I: The scalar case. IMA J Numer Anal 2005;25(4):726–49.
[34] Irwin GR. Analysis of stresses and strains near the end of a crack traversing a plate. SPIE Milestone Ser MS 1957;137:167–70.
[35] Irwin GR. Linear fracture mechanics, fracture transition, and fracture control. Eng Fract Mech 1968;1(2):241–57.
[36] Jonathan RS. Adaptive precision floating-point arithmetic and fast robust geometric predicates. Disc Comput Geom 1997;18(3):305–63.
[37] Kaczmarczyk Ł, Nezhad MM, Pearce C. Three-dimensional brittle fracture: configurational-force-driven crack propagation. Int J Numer Meth Eng 2014;97(7):531–50.
[38] Khoei AR, Azadi H, Moslemi H. Modeling of crack propagation via an automatic adaptive mesh refinement based on modified superconvergent patch recovery technique. Eng Fract Mech 2008;75(10):2921–45.
[39] Ladevèze P, Pled F, Chamoin L. New bounding techniques for goal-oriented error estimation applied to linear problems. Int J Numer Meth Eng 2013;93(13):1345–80.
[40] Larsson R, Fagerström M. A framework for fracture modelling based on the material forces concept with XFEM kinematics. Int J Numer Meth Eng 2005;62(13):1763–88.
[41] Legrain G, Moës N, Verron E. Robust and direct evaluation of J2 in linear elastic fracture mechanics with the X-FEM. Int J Numer Meth Eng 2008;76(10):1471–88.
[42] Li FZ, Shih CF, Needleman A. A comparison of methods for calculating energy release rates. Eng Fract Mech 1985;21(2):405–21.
[43] Liebowitz H, Moyer Jr. ET. Finite element methods in fracture mechanics. Comput Struct 1989;31(1):1–9.
[44] Liebowitz H, Sandhu JS, Lee JD, Menandro FCM. Computational fracture mechanics: research and application. Eng Fract Mech 1995;50(5–6):653–70.
[45] Liu XY, Xiao QZ, Karihaloo BL. XFEM for direct evaluation of mixed mode SIFs in homogeneous and bi-materials. Int J Numer Meth Eng 2004;59(8):1103–18.
[46] Ma GW, An XM, Zhang HH, Li LX. Modeling complex crack problems using the numerical manifold method. Int J Fract 2009;156(1):21–35.
[47] Maugin GA. Material force: concepts and applications. Appl Mech Rev 1995;23:213–45.
[48] Maugin GA. Configurational forces: thermomechanics, physics, mathematics, and numerics. CRC Press; 2016.
[49] Maugin GA, Trimarco C. Pseudomomentum and material forces in nonlinear elastic: variational formulations and applications to brittle fracture. Acta Mech 1992;94:1–28.
[50] Menouillard T, Belytschko T. Analysis and computations of oscillating crack propagation in a heated strip. Int J Fract 2011;167(1):57–70.
[51] Miehe C, Gürses E. A robust algorithm for configurational-force-driven brittle crack propagation with r-adaptive mesh alignment. Int J Numer Meth Eng 2007;72(2):127–55.
[52] Miehe C, Gürses E, Birkle M. A computational framework of configurational-force-driven brittle fracture based on incremental energy minimization. Int J Fract 2007;145(4):245–59.
[53] Min JB, Bass JM, Spradley LW. Adaptive finite element methods for two-dimensional problems in computational fracture mechanics; 1994.
[54] Moës N, Dolbow J, Belytschko T. A finite element method for crack growth without remeshing. Int J Numer Meth Eng 1999;46(1):131–50.
[55] Mueller R, Maugin GA. On material forces and finite element discretizations. Comput Mech 2002;29(1):52–60.
[56] Murthy KSRK, Mukhopadhyay M. Adaptive finite element analysis of mixed-mode crack problems with automatic mesh generator. Int J Numer Meth Eng 2000;49(8):1087–100.
[57] Pled F, Chamoin L, Ladevèze P. An enhanced method with local energy minimization for the robust a posteriori construction of equilibrated stress fields in finite element analyses. Comput Mech 2012;49(3):357–78.
[58] Prudhomme S, Pascal F, Oden JT, Romkes A. Review of a priori error estimation for discontinuous Galerkin methods; 2000.
[59] Rajagopal A, Sivakumar SM. A combined r-h adaptive strategy based on material forces and error assessment for plane problems and bimaterial interfaces. Comput Mech 2007;41(1):49–72.
[60] Raju IS, Shivakumar KN. An equivalent domain integral method in the two-dimensional analysis of mixed mode crack problems. Eng Fract Mech 1990;37(4):707–25.
[61] Rice JR. A path independent integral and the approximate analysis of strain concentration by notches and cracks. J Appl Mech 1968;35(2):379–86.
[62] Rice JR. Limitations to the small scale yielding approximation for crack tip plasticity. J Mech Phys Solids 1974;22(1):17–26.
[63] Riviere B. Discontinuous Galerkin methods for solving elliptic and parabolic equations: theory and implementation. SIAM; 2008.
[64] Ronald K. Virtual crack closure technique: history, approach, and applications. Appl Mech Rev 2004;57(2):109–43.
[65] Rüter M, Stein E. Goal-oriented a posteriori error estimates in elastic fracture mechanics. In: Fifth world congress on computational mechanics, Vienna, Austria; 2002.
[66] Rüter M, Stein E. Goal-oriented a posteriori error estimates in linear elastic fracture mechanics. Comput Meth Appl Mech Eng 2006;195(4–6):251–78.
[67] Rüter M, Stein E. Adaptive finite element analysis of crack propagation in elastic fracture mechanics based on averaging techniques. Comput Mater Sci 2004;31(3):247–57.
[68] Shen Y, Lew A. An optimally convergent discontinuous Galerkin-based extended finite element method for fracture mechanics. Int J Numer Meth Eng 2010;82(6):716–55.
[69] Shih CF, Moran B, Nakamura T. Energy release rate along a three-dimensional crack front in a thermally stressed body. Int J Fract 1986;30(2):79–102.
[70] Simpson R. Enrichment of the boundary element method through the partition of unity method for fracture analysis using local and global formulations PhD thesis Durham University; 2010.
[71] Simpson R, Trevelyan J. Evaluation of J1 and J2 integrals for curved cracks using an enriched boundary element method. Eng Fract Mech 2011;78(4):623–37.
[72] Sladek J, Sladek V. Evaluation of T-stresses and stress intensity factors in stationary thermoelasticity by the coservation integral method. Int J Fract 1997;86(3):199–219.
[73] Solin P, Segeth K, Dolezel I. Higher-order finite element methods. CRC Press; 2003.
[74] Stein M, Rüter E, Ohnimus S. Adaptive finite element analysis and modelling of solids and structures. Findings, problems and trends. Int J Numer Meth Eng 2004;60(1):103–38.
[75] Steinmann P, Scherer M, Denzer R. Secret and joy of configurational mechanics: from foundations in continuum mechanics to applications in computational mechanics. ZAMM – J Appl Math Mech/Z Angew Math Mech 2009;89(8):614–30.
[76] Strang G, Fix GJ. An analysis of the finite element method vol. 212. Englewood Cliffs, NJ: Prentice-hall; 1973.
[77] Sukumar N, Belytschko T. Arbitrary branched and intersecting cracks with the extended finite element method. Int J Numer Meth Eng 2000;48(12):1741–60.
[78] Thoutireddy P, Ortiz M. A variational r-adaption and shape-optimization method for finite-deformation elasticity. Int J Numer Meth Eng 2004;61(1):1–21.
[79] Treifi M, Oyadiji SO. Bi-material v-notch stress intensity factors by the fractal-like finite element method. Eng Fract Mech 2013;105:221–37.
[80] Wang Y, Cerigato C, Waisman H, Benvenuti E. XFEM with high-order material-dependent enrichment functions for stress intensity factors calculation of interface cracks using irwin's crack closure integral. Eng Fract Mech 2017;178:148–68.
[81] Wells GN, Sluys LJ. A new method for modelling cohesive cracks using finite elements. Int J Numer Meth Eng 2001;50(12):2667–82.
[82] Westergaard HM. Bearing pressures and cracks. J Appl Mech 1939;6(2):A49–53.
[83] Yau JF, Wang SS, Corten HT. A mixed-mode crack analysis of isotropic solids using conservation laws of elasticity. J Appl Mech 1980;47(2):335–41.
[84] Zienkiewicz OC, Zhu JZ. The superconvergent patch recovery and a posteriori error estimates. Part 1: The recovery technique. Int J Numer Meth Eng 1992;33(7):1331–64.